



BIOCHEMISTRY

Dimerization of a 5-kDa domain defines the architecture of the 5-MDa gammaproteobacterial pyruvate dehydrogenase complex

Sarah Meinhold†, Rafal Zdanowicz†, Christoph Giese, Rudi Glockshuber*

The *Escherichia coli* pyruvate dehydrogenase complex (PDHc) is a ~5 MDa assembly of the catalytic subunits pyruvate dehydrogenase (E1), dihydrolipoamide acetyltransferase (E2), and dihydrolipoamide dehydrogenase (E3). The PDHc core is a cubic complex of eight E2 homotrimers. Homodimers of the peripheral subunits E1 and E3 associate with the core by binding to the peripheral subunit binding domain (PSBD) of E2. Previous reports indicated that 12 E1 dimers and 6 E3 dimers bind to the 24-meric E2 core. Using an assembly arrested E2 homotrimer (E2₃), we show that two of the three PSBDs in the E2₃ dimerize, that each PSBD dimer cooperatively binds two E1 dimers, and that E3 dimers only bind to the unpaired PSBD in E2₃. This mechanism is preserved in wild-type PDHc, with an E1 dimer:E2 monomer:E3 dimer stoichiometry of 16:24:8. The conserved PSBD dimer interface indicates that PSBD dimerization is the previously unrecognized architectural determinant of gammaproteobacterial PDHc megacomplexes.

INTRODUCTION

The pyruvate dehydrogenase complex (PDHc) is a huge multienzyme assembly that links glycolysis with the citric acid cycle in all aerobic organisms. It catalyzes the transfer of an acetyl moiety from pyruvate onto coenzyme A (CoA) to generate acetyl-CoA, thereby maintaining glucose homeostasis and mediating energy production in the cell (1–4). Converting pyruvate, CoA, and nicotinamide adenine dinucleotide (NAD⁺) into carbon dioxide, acetyl-CoA, and reduced form of NAD⁺ (NADH)/H⁺, the entire PDHc reaction cycle comprises a series of five consecutive reactions (1, 5–8).

The overall reaction catalyzed by PDHcs is the same in prokaryotes and eukaryotes and achieved by three distinct catalytic components. Across all domains of life, PDHcs contain the subunit dihydrolipoamide acetyltransferase (E2) that forms the homo- or hetero-oligomeric PDHc core, and the peripheral subunits pyruvate dehydrogenase (E1) and dihydrolipoamide dehydrogenase (E3) that associate with the core (5, 9–11). The E2 subunit is a multidomain protein in which the individual domains are connected by flexible linkers. Specifically, E2 contains one to three lipoyl domains (LDs) in its N-terminal segment, followed by a peripheral subunit binding domain (PSBD) and a C-terminal catalytic domain (CD) that is also responsible for the assembly of the core (2, 11, 12). In Gram-negative bacteria, PDHc shows a cubic architecture with a core of 24 copies of E2, arranged as eight E2 homotrimers (also termed E2 components) occupying the vertices of the cube (13–15). A cubic core structure is also preserved in the related α -ketoglutarate and branched-chain α -keto acid dehydrogenase complexes (16, 17). Eukaryotic PDHcs have an icosahedral core structure composed of two different subunits, E2 and the E3-binding protein (E3BP), in which E2 only interacts with E1 and E3BP only binds E3 (18, 19). In bacterial PDHcs with cubic core, multiple copies of E1 homodimers and E3 homodimers (E1 and E3 components, respectively) bind to the PSBDs in the flexible N-terminal part of the E2 subunits protruding from the 24-meric core to form an outer protein shell (Fig. 1A). The

peripheral subunits E1 and E3 recognize the overlapping but non-identical binding sites in the small, 5- to 7-kDa PSBD of E2, allowing for interactions with only E1 or E3 in a mutually exclusive manner (20–24).

PDHc from Gram-negative bacteria has been widely reported to comprise a 24-meric E2 core to which approximately 12 E1 dimers and 6 E3 dimers are bound, resulting in a ~4.5-MDa complex (12, 25–28). These data imply that only 18 of the 24 theoretically available PSBD binding sites would be occupied. The role of the potentially remaining six sites has so far not been clarified. For example, other stoichiometries, sometimes largely deviating from the E1:E2:E3 (monomer) ratio of 1:1:0.5, were reported, with the only common denominator that fully assembled PDHc contains twice as many E1 than E3 subunits (29, 30). Up to now, the architectural principle behind the stoichiometry of bacterial PDHcs, the specific arrangement of the peripheral subunits relative to the core, and the reasons underlying the functional advantages of a PDHc megacomplex compared to smaller subcomplexes of E1, E2, and E3 that could conceivably exhibit similar rates of catalysis (31, 32) are unknown. Because of potentially nonuniform subunit compositions and subunit arrangements, as well as the intrinsic flexibility within PDHc subunits required for efficient channeling of catalytic intermediates, no three-dimensional (3D) structure of a fully assembled PDHc (E2 core saturated with the peripheral subunits E1 and E3) is available to date at high resolution. Although atomic resolution models have been solved for the individual components E1 (21, 33), E2 (13, 14, 34, 35), and E3 (20, 23). Recent advances in cryo-electron microscopy and cryo-electron tomography, however, suggested a model wherein the peripheral subunits are flexibly tethered to the core and cluster around the vertices of the E2 cube (14, 36, 37).

Here, we present a biochemical, biophysical, and structural analysis of PDHc from *Escherichia coli*. Our work focused on the generation and characterization of a minimal PDHc composed of a homotrimeric E2 variant whose oligomerization beyond trimers is arrested and which can be fully saturated with E1 dimers and/or E3 dimers. By combining analytical size exclusion chromatography (SEC), analytical ultracentrifugation, optical spectroscopy, enzymatic assays, x-ray crystallography, negative staining electron microscopy (NS-EM) and cryogenic electron microscopy (cryo-EM),

ETH Zürich, Institute of Molecular Biology and Biophysics, Otto-Stern-Weg 5, 8093 Zürich, Switzerland.

*Corresponding author. Email: rudi@mol.biol.ethz.ch

†These authors contributed equally to this work.

Copyright © 2024 the Authors, some rights reserved; exclusive licensee American Association for the Advancement of Science. No claim to original U.S. Government Works. Distributed under a Creative Commons Attribution NonCommercial License 4.0 (CC BY-NC).

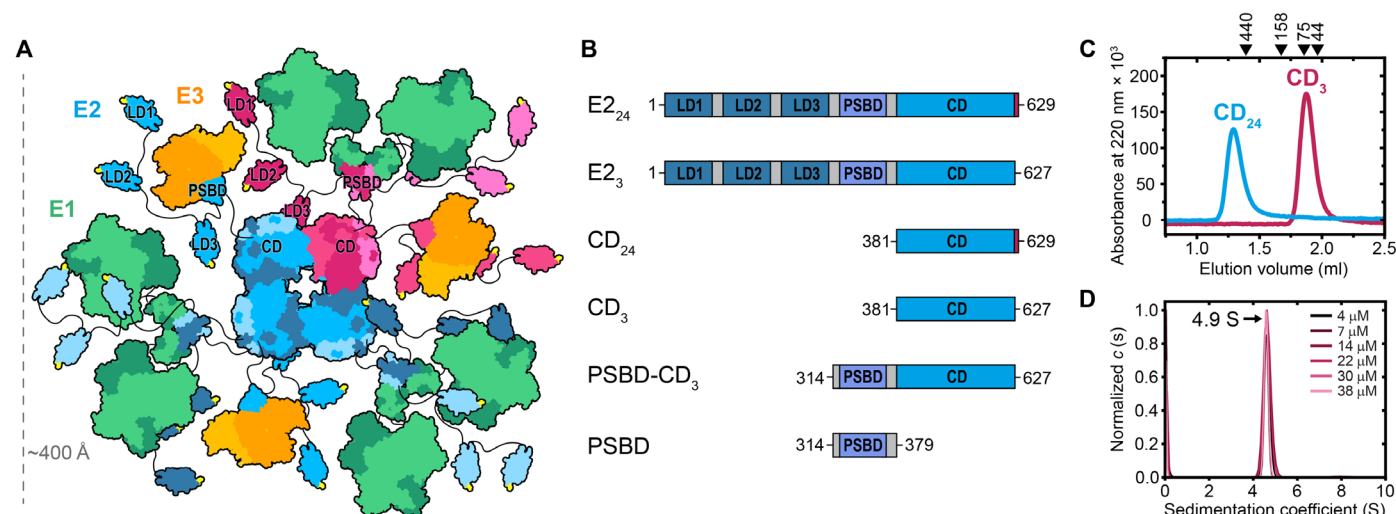


Fig. 1. Simplified model of *E. coli* PDHc, domain organization of the E2 constructs, and assessment of the oligomeric state of CD₂₄ and CD₃ at pH 7.4. (A) Cartoon representation of *E. coli* PDHc. E1 and E3 homodimers form a peripheral protein shell around the cubic E2 core by associating with the PSBD of E2. Models used were as follows: 24-mer of E2 CDs [shades of blue, representative trimeric unit colored red; PDB: 1EAB (15)], E1 with E2 PSBD [green and blue; PDB: 4QOY (21)], E3 with E2 PSBD [orange and blue; PDB: 1EBD (20)], and LDs (LD1 to LD3) of E2 [blue or red; PDB: 1QJO (83)]. Black lines correspond to the flexible linkers between the domains of each E2 subunit. Note that the cartoon does not provide specific information on the dynamics, exact subunit composition and interaction network within PDHc. (B) Domain organization of full-length *E. coli* E2 (E2₂₄) and truncated E2 variants. Flexible linker regions are depicted in gray. (C) Analytical SEC on Superdex 200 Increase 5/150 GL (3 ml volume) of CD₂₄ (blue) and CD₃ (red) recorded at 220 nm. The profiles are consistent with the homotrimeric state of CD₃ within experimental error. Elution volumes of molecular mass standard proteins (in kDa) are indicated. (D) SV-AUC analysis of CD₃ at pH 7.4 and 20°C. Normalized sedimentation coefficient distributions *c* (s) for the indicated initial CD₃ concentrations are shown. In the tested concentration range, a single CD₃ species at 4.9 S was observed, confirming homogeneity of the preparation.

we show that this minimal ~700-kDa complex (mini-PDHc) harbors all structural principles determining the stoichiometry of wild-type PDHc (~5 MDa) and already has enzymatic activity comparable to that of the wild-type complex. In addition, we confirm that the E1 dimer:E2 monomer:E3 dimer ratio of 2:3:1 found for mini-PDHc is preserved in the wild-type complex. Specifically, this subunit composition is the consequence of a previously unknown dimerization reaction between PSBD domains within each E2 homotrimer: While two E1 dimers associate with dimeric PSBD, E3 exclusively interacts with the remaining unpaired PSBD. This balance ensures sufficient E1 binding in the presence of excess E3 and sufficient E3 binding at excess of E1. Last, on the basis of sequence conservation analysis, we propose that this mechanism is conserved across Gammaproteobacteria, rendering the structural principles in *E. coli* PDHc applicable to PDHcs in a multitude of other species, including medically relevant human pathogens such as *Pseudomonas aeruginosa*, *Salmonella enterica*, or *Vibrio cholerae*.

RESULTS

A two residue, C-terminal truncation of E2 yields a stable E2 trimer

Structural studies on the 24-meric wild-type E2 core (E2₂₄) from *E. coli* had been hampered by its size and the flexibility of the N-terminal E2 domains. As only the CD of E2 contributes to the assembly of the E2₂₄ core complex, we created a truncated construct of wild-type E2 by deleting all LDs (LD1 to LD3) and PSBD of E2. We will refer to this construct, spanning E2 residues 381 to 629, as CD₂₄. To arrest oligomerization beyond trimers, we further deleted the two C-terminal residues V628 and M629 that are involved in intertrimer interactions

(13, 14). This CD variant comprises residues 381 to 627 and will be referred to as CD₃ (see Fig. 1B for nomenclature and domain organization of all E2 constructs used in this study). Analytical SEC revealed a single peak corresponding to a considerably smaller hydrodynamic radius of CD₃ compared to CD₂₄, which was consistent with the homotrimeric state of CD₃ within experimental error (Fig. 1C and fig. S1). To assess homogeneity and to confirm the trimeric oligomerization state of CD₃, we performed sedimentation velocity analytical ultracentrifugation (SV-AUC) experiments with different initial CD₃ concentrations. For all samples, a single species was observed, with a sedimentation coefficient at 20°C and infinite dilution in water (*s*_{20,w}⁰) of 4.87 ± 0.01 S (Fig. 1D). Using sedimentation equilibrium AUC (SE-AUC), the molecular mass of the CD₃ complex was determined to 79.8 ± 0.4 kDa (fig. S2), confirming that CD₃ was indeed a homotrimer in solution (calculated molecular mass of CD₃: 82.1 kDa). Far-ultraviolet (UV) circular dichroism spectra and co-operative, temperature-induced unfolding transitions indicated that both CD₃ and CD₂₄ adopted well-defined folds (fig. S3, A and B).

To confirm that the E2 fold was preserved in CD₃ and to reveal the structural basis of its arrested assembly to a 24-mer, we crystallized the protein and solved its structure at 1.97-Å resolution with molecular replacement using an *E. coli* E2 model [Protein Data Bank (PDB): 4N72 (38)] (Fig. 2A). In addition, for a direct reference to our CD₃ structure, we determined the cryo-EM structure of CD₂₄ and reconstructed the map to 3.3-Å global resolution with local resolution estimates between 2.7 and 3.5 Å (Fig. 2B). As expected, our analysis yielded a cubic assembly composed of eight E2 homotrimers, each situated at the vertices of the cubic complex. The two models of CD₃ and CD₂₄ resemble the previously published trimer structure by Wang *et al.* (38) with an average root mean square

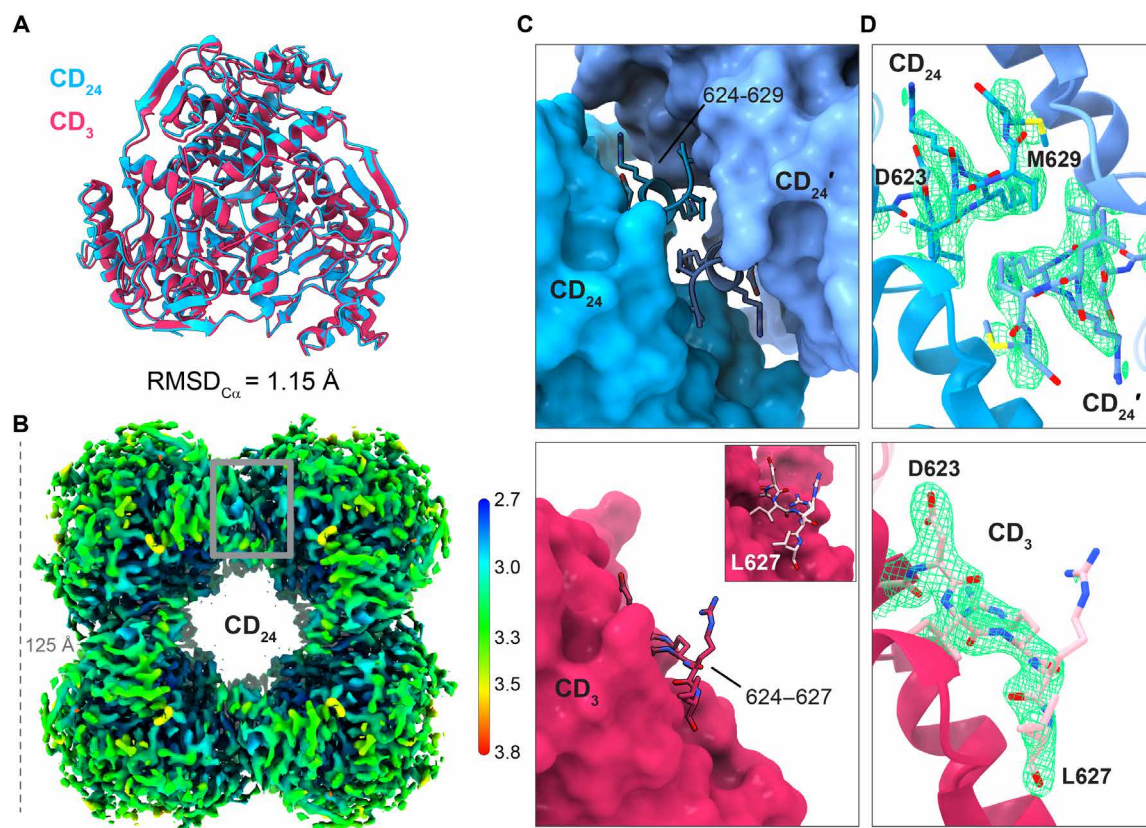


Fig. 2. Structures of the CD₂₄ and CD₃ complexes. (A) Overlay of CD₃ (red) and a trimeric unit of CD₂₄ (blue), demonstrating the two structures as highly similar. The RMSD_{Cα} is provided. (B) Cryo-EM map of the CD₂₄ complex at 3.3-Å resolution. The map is colored according to the local resolution estimates (color key provided; Å). The interior part of the cube was reconstructed at about 2.7-Å resolution, while the exterior region was refined to 3.0- to 3.5-Å resolution. The trimer-trimer interface is highlighted with a gray box. (C) Interface between neighboring trimers in CD₂₄ (top) and the corresponding view of CD₃ (bottom). In the cubic CD₂₄ complex, the two neighboring trimers form a conserved E2 knob-into-hole interaction. Residues 624 to 629 (side chains shown) form the 3_{10} -helix that binds in the hydrophobic pocket of a neighboring trimer. This interaction is abolished in the trimeric CD₃, where the C-terminal L627 binds the hydrophobic groove of the same monomer (magnified view in the bottom panel). (D) cryo-EM and electron density maps for the C-terminal segments of CD₂₄ (top) and CD₃ (bottom), respectively.

deviation for all alpha carbons (RMSD_{Cα}) per monomer of 1.01 and 0.62 Å, respectively. Both of our structures have a virtually identical CD fold with an RMSD_{Cα} of 1.15 Å (Fig. 2A), indicating that the removal of the last two amino acid residues neither impaired folding of the CD nor its association to trimers but only inhibited 24-mer formation.

The biochemical and structural data showed that the small, C-terminal two-residue truncation was sufficient to completely prevent intertrimer contact formation and further oligomerization to large, cubic complexes. Our CD₂₄ model confirmed a conserved “knob-into-hole” interaction between the neighboring E2 trimers (Fig. 2, C and D, top panels), as first described by Mattevi *et al.* (13). Here, residues 624 to 629 of one trimer form the short C-terminal 3_{10} -helix (knob) that fits into a hydrophobic pocket in a neighboring trimer (hole). Notably, the deletion of V628 and M629 in CD₃ prevented further oligomerization via a different mechanism: It breaks the C-terminal 3_{10} -helix, causing residues 624 to 627 to remain in an extended conformation and allowing L627 to dock intramolecularly into the hydrophobic groove that would be occupied by V628 and M629 of a neighboring trimer in wild-type E2₂₄ (Fig. 2, C and D, bottom panels). This mechanism of arrested assembly differs

from that in a previously reported CD trimer, in which further assembly was prevented sterically via a C-terminal peptide extension (38).

The complex formed between E2, E1, and E3 has a defined stoichiometry

To determine the binding stoichiometry of the peripheral subunits to trimeric E2, we used a C-terminally truncated variant of E2 (E2₃, residues 1 to 627) analogous to CD₃ but still retaining the LD domains LD1 to LD3 and the PSBD domain. We analyzed E2₃ for its ability to associate with E1 dimers and E3 dimers using analytical SEC. The same approach was used in parallel for the wild-type E2₂₄ core to directly compare the assembly of E2₃ and E2₂₄ with the peripheral subunits. The results are summarized in Table 1 and Fig. 3.

When E2₂₄ (constant concentration) was titrated with E1 alone, saturation was reached at 22.3 bound E1 dimers, which is very close and within experimental error to a 1:1 ratio between E2 monomers and E1 dimers. The same titration experiment with constant E2₃ concentration yielded 2.5 E1 dimers bound to E2₃ (Fig. 3A), corresponding to a mixture of complexes with three (saturated) and two

Table 1. Stoichiometry of E1 and E3 binding to E2, indicated as the fraction of occupied E2 monomers after saturation. n.a., not applicable.			
	E1 added	E3 added	
E2 ₃	0.85 ± 0.02	0.87 ± 0.05	
E2 ₂₄	0.93 ± 0.05	0.75 ± 0.04	
E2 ₂₄ -V364K	0.61 ± 0.04*	0.79 ± 0.05	
E2 ₃ -V364K	0.86 ± 0.05	0.89 ± 0.03	

*This value is underestimated due to partial dissociation of the complex during SEC (see fig. S9).

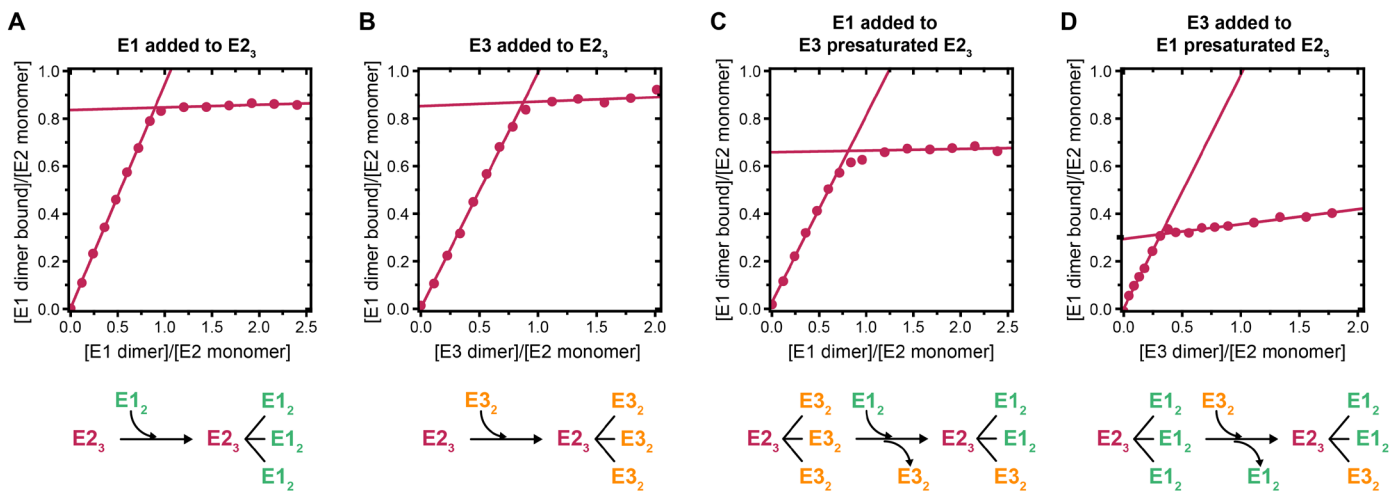


Fig. 3. Binding reactions between the homotrimer E2₃ and the peripheral subunits E1 and E3. The ratio of E1/E3 dimers bound per E2 monomer is plotted against the respective ratio of E1 or E3 dimers added per E2 monomer (ratio of ligands per binding site). The ratio of E1/E3 dimers bound per E2 monomer was calculated from the peak areas of complexed subunits in the respective chromatograms recorded at 280 nm [(A) and (C)] or 450 nm [flavin adenine dinucleotide (FAD) cofactor in E3] [(B) and (D)] and normalized using the total peak area as a calibration curve. (A) Saturation of E2₃ with E1. (B) Saturation of E2₃ with E3. (C) Binding of E1 to the saturated E3:E2₃ subcomplex displaces two E3 dimers. (D) Binding of E3 to the saturated E1:E2₃ subcomplex displaces one E1 dimer.

E1 dimers bound to E2₃. The results thus showed that all PSBD domains in E2₃ and E2₂₄ can be saturated with E1 dimers. Titration of E2₃ and E2₂₄ with E3 alone yielded 2.6 bound E3 dimers for E2₃ and 17.9 bound E3 dimers for E2₂₄ (Fig. 3B). For E2₂₄, the recorded stoichiometry is in good agreement with a previous report by Reed *et al.* (25), where 22 E1 dimers and 19 E3 dimers were found to bind to the E2 24-mer. Next, we investigated the competition between the peripheral subunits E1 and E3 for binding to PSBD in E2. For this purpose, E2₃ or E2₂₄ were presaturated with either E1 or E3 and then titrated with E3 or E1, respectively. The results, shown in Table 1 and Fig. 3, demonstrated that each peripheral subunit could displace the other subunit from the respective presaturated complex. Specifically, we observed an average of 2.0 and 17.1 E1 dimers binding to the saturated E3:E2₃ and E3:E2₂₄ subcomplexes, respectively. Reversely, an average of 0.9 E3 dimers displaced E1 from the E2₃ trimer, while 8.3 E3 dimers associated with the E1:E2₂₄ complex. Figure 3 schematically summarizes the observed displacement reactions and their stoichiometries for E2₃. Together, our analysis of E2₂₄ in complex with E1 and E3 differs from the previously published data on PDHc isolated from its native environment in that the reconstitution of the entire PDHc

from individual, purified subunits demonstrated that, indeed, all 24 PSBD domains of the E2₂₄ core can be saturated with the peripheral subunits: In contrast to the reported stoichiometry of 12 E1 dimers and 6 E3 dimers bound per E2₂₄ (25–28), we found ~16 E1 dimer and ~8 E3 dimer equivalents per E2₂₄ at saturating concentrations of E1 and E3, corresponding to an E1 dimer:E2 monomer:E3 dimer ratio of 2:3:1. Notably, this PDHc subunit ratio could be fully reproduced for the complex of E2₃ saturated with E1 and E3: Fig. 3 (C and D) shows that two E1 dimers and one E3 dimer associated with the E2₃ trimer, forming a complex that we will refer to as mini-PDHc. Consequently, the fully saturated PDHc wild-type complex can be considered a supramolecular structure composed of eight identical mini-PDHc subcomplexes located at the vertices of the cube. Next, we measured the overall enzymatic activity of mini-PDHc relative to wild-type PDHc under nearly saturating concentrations of the three substrates pyruvate, CoA, and NAD⁺ (fig. S3D). Mini-PDHc showed 60% of the wild-type PDHc activity (fig. S3E). This demonstrates that intersubunit exchange of catalytic intermediates and facilitated substrate diffusion are already largely achieved within the mini-PDHc complex, making it a suitable target for further structural investigation.

Structural analysis of mini-PDHc_{ΔLD} reveals PSBD-mediated linkage of two E1 dimers

For further structural characterization of mini-PDHc with SV-AUC and EM, we constructed a simplified E2 variant in which the flexibly attached, N-terminal LDs were deleted (ΔLD). The resulting, homotrimeric variant PSBD-CD₃ (residues 314 to 627; Fig. 1B) retained the ability to bind E1 and E3 at the same molar ratios observed for mini-PDHc (fig. S4). The corresponding complex with two E1 dimers, the PSBD-CD₃ homotrimer, and one E3 dimer will be referred to as mini-PDHc_{ΔLD} in the following. After purification by SEC, mini-PDHc_{ΔLD} sedimented as a single species with a sedimentation coefficient (*s*_{20,w}) of 16 S (Fig. 4A), demonstrating that mini-PDHc_{ΔLD} had a defined stoichiometry. The apparent molecular mass calculated from the sedimentation data was ~530 kDa, consistent with binding of two E1 dimers and one E3 dimer to one trimer of PSBD-CD₃ (calculated mass: 604 kDa).

To gain more structural insight into the interaction between the peripheral subunits and the E2 core, we analyzed mini-PDHc_{ΔLD} by EM. First, the complex was analyzed by NS-EM to assess the order and homogeneity of the particles. 2D class averages obtained during the single-particle analysis revealed two easily distinguishable subpopulations of particles. Under the applied NS-EM conditions, approximately 20% of all particles had two E1 dimers and one E3 dimer bound (Fig. 4B), corresponding to the stoichiometry of mini-PDHc_{ΔLD} as determined via SEC and AUC. The remaining 80% of the particles consisted of two E1 dimers bound to PSBD-CD₃ (Fig. 4C), from which E3 likely had dissociated during EM grid preparation. We consider the loss of E3 an NS-EM artifact, as this dissociation reaction was never observed during SEC or AUC in solution. The classes obtained for the two subpopulations of particles are highly similar and follow an identical pattern: Two E1 dimers are located close to each other, whereas E3 (if present) is more flexibly bound on the side of the trimer of the E2 CDs and separated from the E1 dimers.

In addition to the densities corresponding to E1, E2 CD, and E3, a V-shaped structure was observed between the E1 dimers and the E2 CD trimer. This density appeared to orient the two E1 dimers in a defined relative orientation and to prevent more random, unrestrained E1 arrangements. The location of this density and the observation of apparent bridging between the E1 and the E2 subunits suggested that the structure corresponded to two associated PSBD domains within PSBD-CD₃ (Fig. 4, B and C).

Analysis of the low-resolution maps of mini-PDHc_{ΔLD} with (Fig. 4D) and without (Fig. 4E) the E3 component showed that all densities observed in 2D were resolved well enough to fit crystal structures of the individual proteins. The estimated distances between E1 dimers or E3 dimers and the E2 CD trimer were approximately 50 to 60 Å. This is in agreement with the sum of folded PSBD (~32 Å) (21) and the length of the flexible, 11-residue linker connecting the PSBD with the CD (~38 Å for the fully extended linker, E2 residues 374 to 384).

The PSBD density observed in our 2D class averages could also be resolved in 3D demonstrating a clear connection between the two bound E1 dimers. Despite the low resolution, the continuous density observed here suggested an interaction mechanism in which two of the three PSBDs of PSBD-CD₃ dimerize, the PSBDs in the dimer preferentially bind E1 dimers, and the remaining unpaired PSBD preferentially bind an E3 dimer.

Homodimeric PSBD binds two E1 dimers

To analyze a putative dimerization of PSBD, we recombinantly produced the isolated PSBD domain spanning E2 residues 314 to 379 and characterized the protein structurally via x-ray crystallography and EM.

The crystal structure of PSBD was solved to 1.64-Å resolution. As predicted from our EM analysis, PSBD indeed associated to a V-shaped homodimer (Fig. 5A and fig. S5) formed by two parallel α helices (residues 331 to 339 and 357 to 372) from each monomer that are connected with a 19-residue long loop. Our refined model closely resembles the available crystal structure of monomeric PSBD from *Geobacillus stearothermophilus*, with RMSD_{Cα} of 0.74 Å (39). While the N-terminal region of PSBD (residues 327 to 334 and 350 to 354) had been shown to interact with peripheral subunits (20, 21), our crystal structure showed that the more C-terminal PSBD segment (residues 335 to 339 and 360 to 368) is responsible for dimer formation. Hydrophobic residues line the interface between the PSBD monomers, indicating that a network of hydrophobic interactions holds them together, with a buried surface area of 872 and 844 Å² per monomer according to PDBePISA (40) and COCOMAPS (41), respectively (Fig. 5B). The amino acid residues identified as key contributors to the hydrophobic interface include F339, V364, and I368 (Fig. 5C). Furthermore, SE-AUC showed that purified PSBD is a homodimer in solution with an experimentally determined mass of 14.0 ± 0.1 kDa (calculated mass of the dimer: 14.6 kDa, fig. S6). Given that PSBD monomers were not detected by SV-AUC even at the lowest PSBD concentration used (8.9 μM PSBD monomer), we can estimate an upper limit for the dissociation constant (*K*_D) of the isolated PSBD dimer of ~0.1 to 1.0 μM.

Next, we used NS-EM to investigate whether isolated PSBD can interact with E1 and if this interaction occurs between two E1 dimers, analogous to mini-PDHc_{ΔLD}. The 2D class averages revealed that the E1:PSBD complex shows a characteristic pattern of two densities held close to each other (Fig. 5D). While the strong density bridging the E1 subunits further confirmed the ability of dimeric PSBD to associate with two E1 dimers, the complex appeared conformationally heterogeneous due to variable distances between the E1 dimers.

To gain higher resolution, we attempted to solve the structure of mini-PDHc_{ΔLD} using cryo-EM. Because of the flexible linker between PSBD and CD, chemical crosslinking with bis-(succinimidyl) suberate (BS³) was used to visualize the preferred conformational states of the particles and to improve resolution. The obtained 2D class averages showed that the E3 component could not be crosslinked to PSBD and dissociated, possibly upon freezing (Fig. 5E). The two E1 dimers, flexibly connected with the PSBD dimer, adopted two main, symmetrical conformations in the complex and were either very close to each other, almost touching, or fully separated (Fig. 5E). The 2D alignments were driven primarily by PSBD-linked E1 dimers, so that the density for CD₃ appeared blurry, indicating considerable conformational freedom within the complex.

Focusing the alignments on a single E1 dimer to later extend onto PSBDs not only allowed us to reconstruct dimeric E1 at ~4-Å global resolution but also revealed a high degree of heterogeneity in the dataset (fig. S7). As expected, the estimated local resolution of our map was nonuniform, where the E1 dimer was refined to 3.5 to 6 Å while the density for PSBD was reconstructed to 6- to 10-Å resolution (Fig. 5F). For model fitting, we used AlphaFold (42, 43) to predict a

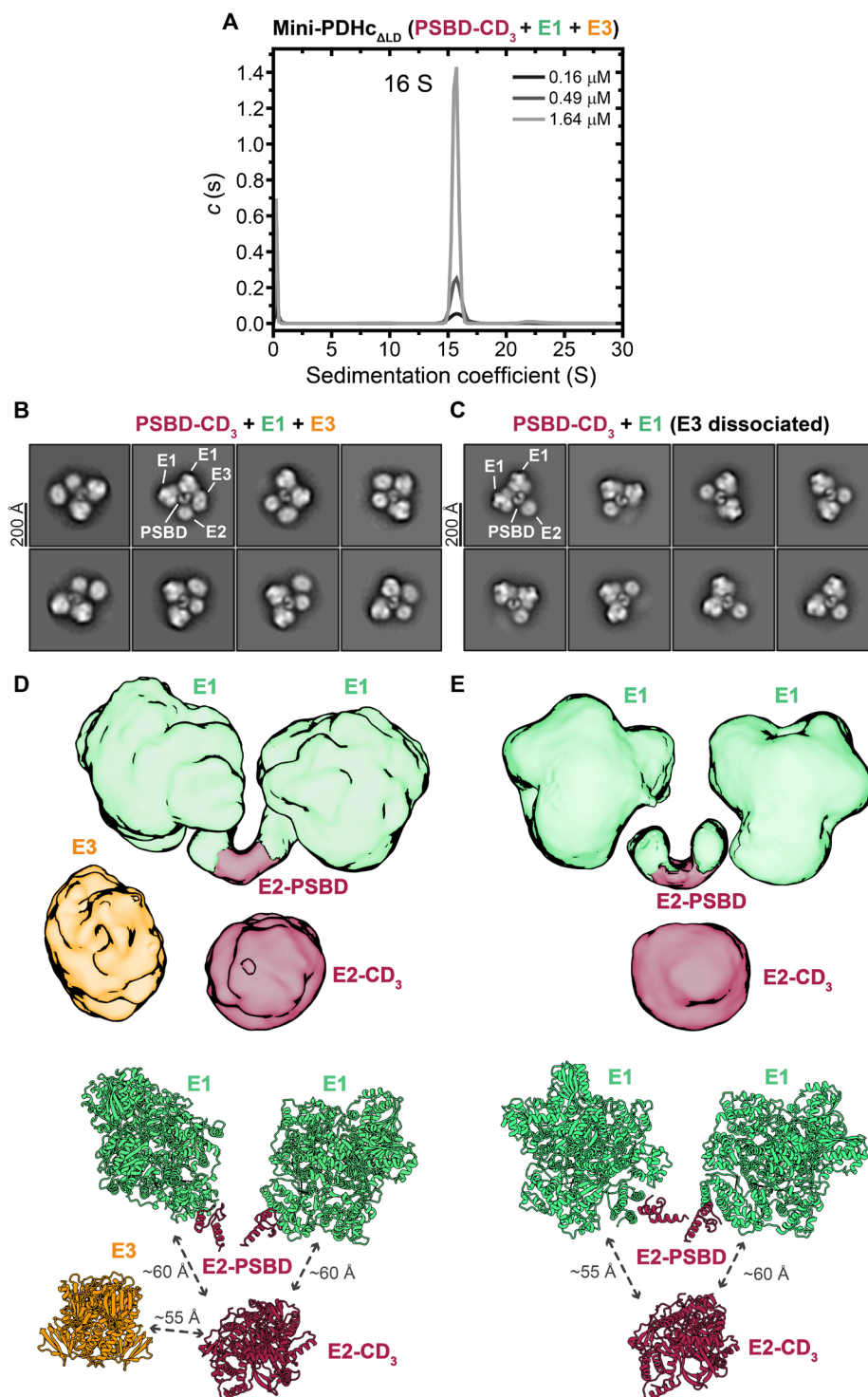


Fig. 4. SV-AUC and NS-EM analyses of mini-PDHc_{ΔLD}. (A) Sedimentation coefficient distributions c (s) of mini-PDHc_{ΔLD}. The initial concentrations of the complex and the calculated sedimentation coefficient $s_{20,w}$ are indicated. Data were recorded at 20°C, pH 7.4. (B) Selection of 2D class averages generated for a subset of particles where E3 remained bound (mini-PDHc_{ΔLD}). Protein components are labeled. (C) Selection of 2D class averages for a subset of particles from which E3 dissociated. Protein components are labeled. (D and E) NS-EM density maps of mini-PDHc_{ΔLD} (D) and mini-PDHc_{ΔLD} from which E3 dissociated (E) colored in green (E1), red (E2), and orange (E3) according to the identity of the complex subunit. Crystal structures of *E. coli* E1 with PSBD [PDB: 4QOY (27)], *E. coli* E3 [PDB: 4JDR (23)], and CD₃ of *E. coli* E2 were fitted into the maps using UCSF ChimeraX (model map correlations of 0.88 to 0.92 at 15-Å resolution) and are shown below the maps. Approximate distances between the proteins are indicated.

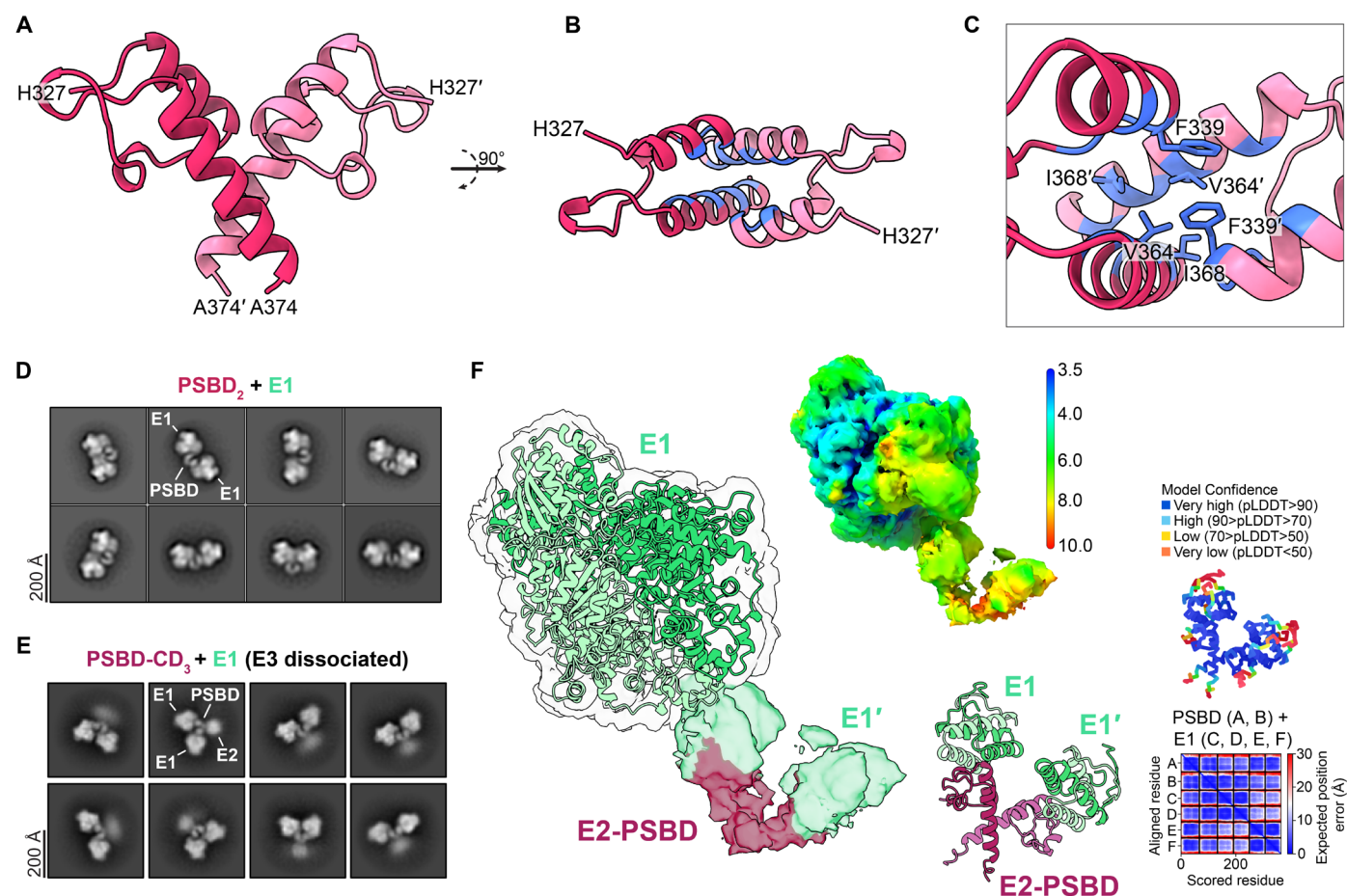


Fig. 5. Structure of *E. coli* PSBD homodimer and its binding to two dimers of E1. (A) Crystal structure of the dimeric PSBD of *E. coli* E2 at 1.64-Å resolution. The two monomers are colored red and pink, respectively. (B) Top view of the crystal structure shown in (A). Hydrophobic residues stabilizing a dimer interface are colored blue. (C) Magnified view of the hydrophobic interface shown in (B). The residues with two or more hydrophobic contacts within <4-Å distance are labeled. (D) NS-EM 2D class averages obtained for PSBD complexed with E1. Dimeric PSBD associates with two E1 dimers. Each density is identified for one class. (E) Cryo-EM 2D class averages of the B5³-crosslinked mini-PDHc_{ΔLD}. (F) Model of the complex between one E1 dimer and the PSBD dimer, rigid-body fitted into the cryo-EM map after 3D variability analysis and local refinement. The nontransparent map is shown on the right and colored according to local resolution estimates. Models used were as follows: PDB: 4QOY (E1 residues 56 to 886) and AlphaFold prediction of four E1 chains (residues 1 to 58) in complex with two PSBD chains (E2, residues 314 to 379). A downsized copy of the AlphaFold model, colored according to per-residue confidence score [predicted local distance difference test (pLDDT)], and the predicted aligned error plot are provided. The low-confidence regions correspond to disordered linkers between PSBD and CD of E2 and between the N-terminal PSBD-binding E1 segment and the rest of the E1 dimer.

model of four E1 chains (E1 segments 1 to 58) in complex with two PSBD chains (E2 residues 314 to 379). This model and the crystal structure of the E1 dimer (PDB: 4QOY, residues 56 to 886) were rigid-body fitted into the map. While the E1 structure fitted well into the EM density reconstructed at ~4-Å resolution, the fit of the AlphaFold model was more ambiguous within the less resolved region. Nevertheless, the E1:PSBD model presented here is in good agreement with the observations made from 2D class averages and explains how dimeric PSBD not only bridges between E1 and E2 but also brings the two E1 dimers into close proximity.

PSBD dimerization is likely conserved in PDHcs of Gammaproteobacteria

So far, PSBD of bacterial E2 subunits had only been described as a monomeric domain (34, 44–46). We therefore investigated the degree of sequence conservation among the prokaryotic PDHcs. On

the basis of AlphaFold predictions, we hypothesized that the PSBD dimerization mechanism observed for *E. coli* E2 may be intrinsic to gammaproteobacterial PDHcs. PSBD sequence analysis revealed a high overall sequence similarity (more than ~60% relative to *E. coli* PSBD) within this class of bacteria and near 100% conservation of the residues forming the contacts with E1 or E3 (H327, P330, R333, R337, and R354). Thus, the mode of interaction between E2 and the peripheral subunits observed in *E. coli* PSBD is likely preserved within Gammaproteobacteria (Fig. 6, A and B). The PSBD residues V364 and K365 also show near full sequence conservation. They are positioned in the middle of the second helix, distant from the binding interface with E1 or E3, indicating that they might play a role in PSBD dimerization. Furthermore, the C-terminal stretch of PSBD comprising residues 366 to 374 is presumed to elongate the helix and further stabilize PSBD dimers, given that the hydrophobic nature of amino acids pointing inward (A367, I368, and A371) is generally

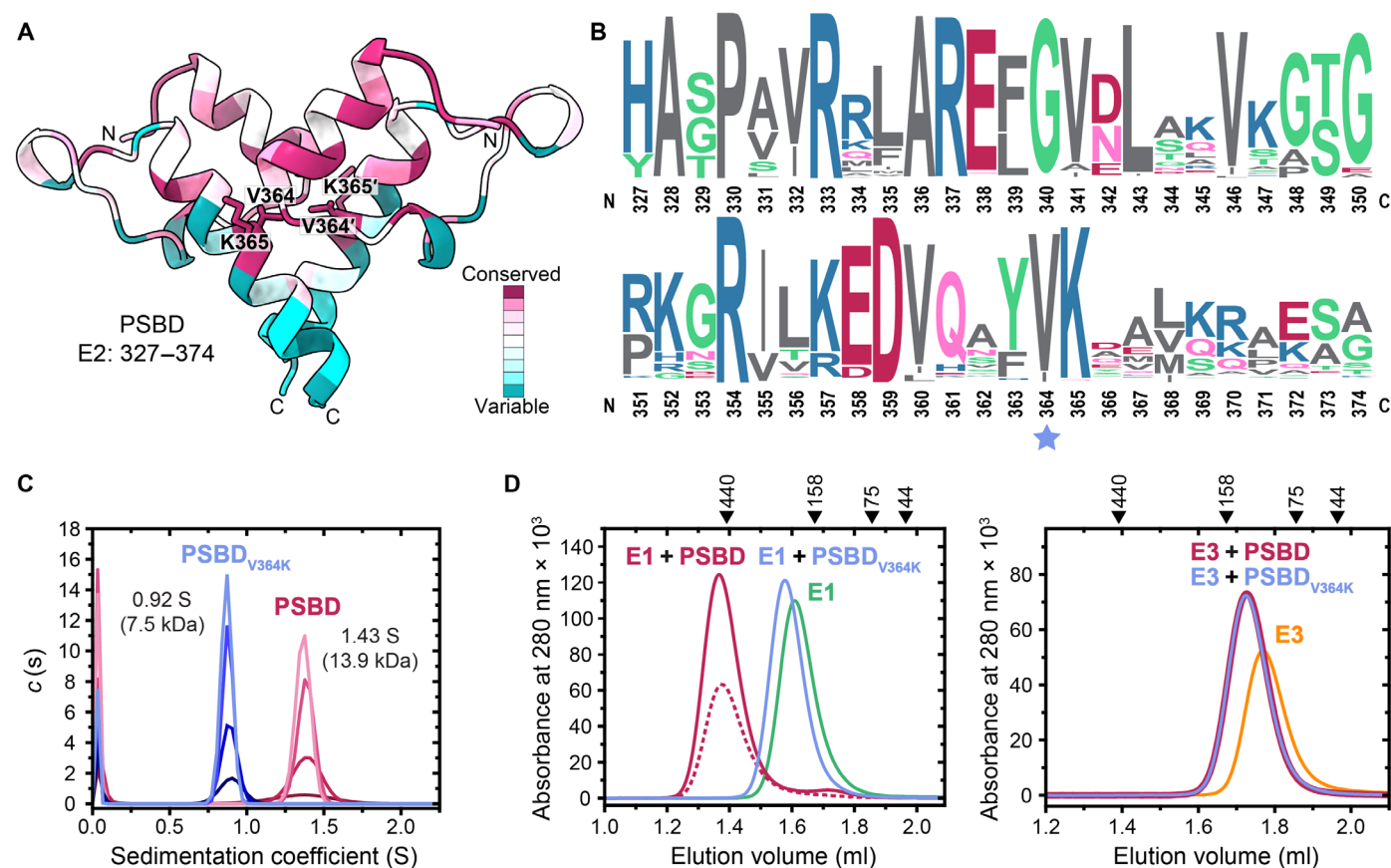


Fig. 6. PSBD sequence conservation and its interactions with the peripheral subunits E1 and E3. (A) Crystal structure of the *E. coli* PSBD colored according to the degree of conservation among Gammaproteobacteria. The highly conserved residues, V364 and K365, which are not involved in binding E1 or E3, are labeled. (B) Sequence logo plot representing the per-residue conservation within PSBD. The highly conserved V364 is marked with a star symbol to highlight the site of substitution with lysine in the PSBD_{V364K} variant. (C) Sedimentation coefficient distributions $c(s)$ of PSBD (red) and PSBD_{V364K} (blue) for 8.9 to 37 μ M protein (monomer concentration). Calculated sedimentation coefficients $s_{20,w}$ are indicated. Data were recorded at 20°C, pH 7.4. (D) Analytical SEC performed on the PSBD variants complexed with E1 (left) or E3 (right). Elution volumes of molecular mass standard proteins (in kDa) are indicated. The monomeric PSBD_{V364K} binds to a single dimer of either E1 or E3. Dimeric PSBD associates with two dimers of E1, whereas E3 binds to monomeric PSBD. Dashed line denotes elution profile of an equimolar mixture of E1 dimers and PSBD dimers. All E1 dimers accumulated in the peak corresponding to the complex of two E1 dimers bound to dimeric PSBD, showing that E1 binding is cooperative.

conserved. Another key residue of the hydrophobic PSBD dimer interface is F339, which is either a phenylalanine or leucine in gammaproteobacterial PSBDs.

To confirm the role of V364 as a critical residue in the hydrophobic interface of the PSBD dimer, we substituted V364 with lysine in the variant PSBD_{V364K}. SV-AUC analysis showed that PSBD_{V364K} sedimented as a uniform monomer with $s_{20,w}$ of 0.92 S and apparent molecular mass of ~7.5 kDa (calculated mass 7.3 kDa) compared to $s_{20,w}$ of 1.43 S and ~13.9 kDa determined for dimeric PSBD (calculated mass 14.6 kDa) (Fig. 6C).

To test if the V364K substitution in PSBD affected the interaction between PSBD and the peripheral subunits, we performed analytical SEC runs for the complexes between E1 or E3 and either the PSBD dimer or the PSBD_{V364K} monomer (Fig. 6D). The samples of E1 complexed with the two PSBD variants yielded distinct chromatograms. While only a small shift toward higher mass was observed in the elution profile of the E1 dimer (~200 kDa) after the addition of PSBD_{V364K} (~7-kDa mass increase due to binding of PSBD_{V364K}), the retention volume of the complex between the

PSBD dimer and E1 indicated formation of two E1 dimers binding per PSBD dimer (Fig. 6D, left). This is in full agreement with the EM data described above, where particles of two E1 dimers linked by dimeric PSBD were detected (Fig. 5D). In contrast, E3 showed small, essentially identical peak shifts toward higher mass when incubated with the PSBD dimer or the PSBD_{V364K} monomer (Fig. 6D, right). This demonstrates that E3 dimers form stable complexes exclusively with PSBD monomers.

Notably, analytical SEC also revealed that E1 binds cooperatively to the PSBD dimer. Specifically, when E1 was mixed with an equimolar amount of PSBD dimers, all E1 dimers accumulated in the saturated complex (two E1 dimers per PSBD dimer), while no complexes comprising only a single E1 dimer could be detected. This demonstrates that binding of the first E1 dimer to dimeric PSBD strongly favors binding of the second E1 dimer (Fig. 6D, left).

For a further analysis of the PSBD:E3 interaction, complexes between E3 dimers and either one or two PSBD chains were modeled using AlphaFold. A structure of the E3₂:PSBD₁ complex (single PSBD chain) could be predicted with high confidence and in good

agreement with the crystal structure from *G. stearothermophilus* (20) where PSBD was shown to bind as a monomer at the dimer interface of E3 (fig. S8A). Although symmetric E3 homodimers have two potential binding sites for monomeric PSBD, these cannot be occupied simultaneously by two PSBD chains due to steric clashes (fig. S8B). In contrast, the N-terminal region of PSBD responsible for E3 binding was predicted with considerably lower confidence for E3₂:PSBD₂ (two PSBD chains) (fig. S8, C and D), as the second chain of the PSBD dimer caused steric hindrance preventing it from interacting with the native binding site of the E3 dimer. In conclusion, the AlphaFold models described above support our SEC and EM data and point to monomeric PSBD as the single binding target for E3.

Dimerization of PSBD dictates PDHc stoichiometry

On the basis of the above results, we hypothesized that PSBD dimerization within an E2 homotrimer is the critical determinant for the subunit composition of *E. coli* PDHc and possibly many other gammaproteobacterial PDHcs. To test this hypothesis, we introduced the V364K substitution into E2₂₄ and E2₃ to disrupt the PSBD dimerization interface and analyzed the resulting E2₂₄-V364K and E2₃-V364K variants for complex formation with the peripheral subunits using analytical SEC (Table 1, Fig. 7, and fig. S9). The results demonstrated that E1 and E3 subunits exhibit different preferences toward monomeric and dimeric PSBD. While E1 dimers bind preferentially to dimeric PSBD, E3 displaces only E1 dimers associated with monomeric PSBD.

As expected for a blocked PSBD dimerization in the V364K variants of E2 and the inability of E3 to bind dimeric PSBD, we observed no notable differences between wild-type and mutant E2 constructs in their maximum occupancy with E3 dimers (one E3 dimer per E2 monomer; Table 1 and Fig. 7E). For binding of E1, however, the occupancy of E2 monomers in E2₂₄-V364K at a 2.5-fold excess of E1 dimers dropped from 93% (E2₂₄ wild-type) to 61% (Fig. 7A and Table 1). The titration profile for E2₂₄-V364K also showed a clear curvature, indicative of weaker binding of E1 dimers to monomeric PSBD in E2₂₄-V364K (Fig. 7A) and possibly dissociation of E1 from the complex during SEC (fig. S9). The preference of E1 dimers for dimeric compared to monomeric PSBD is best illustrated by the observation that E1 can no longer displace E3 from PSBD monomers in E2₂₄-V364K or E2₃-V364K (Fig. 7, B to D, and Table 1). Conversely, E3 dimers essentially displaced all E1 dimers from E2₂₄-V364K or E2₃-V364K (Fig. 7, F and G, and Table 1), while two of three E1 dimers remained bound in wild-type E2₂₄ or E2₃ at an excess of E3 (Fig. 7H and Table 1).

From the presented data, we conclude that two E1 dimers are strongly bound to dimeric PSBD in E2₃ fully saturated with E1 dimers, and one E1 dimer is bound weakly to the remaining unpaired PSBD. Only this weakly bound E1 dimer can then be displaced by an E3 dimer, yielding a final E1 dimer: E2 monomer: E3 dimer ratio of 2:3:1 (Fig. 7H). This mechanism also guarantees that the 2:3:1 ratio is maintained at oversaturation with E1 or E3 dimers. The preferred binding of two E1 dimers to a PSBD dimer and the exclusive binding of E3 dimers to monomeric PSBD is also consistent with the fact that an E1:E3 ratio of 2:1 was found in most previous reports on the stoichiometry of *E. coli* PDHc in the majority of which the face/edge model of PDHc was assumed (10, 12, 25, 27, 29).

DISCUSSION

Over the last decades, numerous reports provided important mechanistic and structural insights into the multienzyme assembly of *E. coli* PDHc (14, 23, 33–37, 47). The biochemical, biophysical, and structural analyses of wild-type PDHc and its minimized variant mini-PDHc presented here allowed us to gain more detailed insight into the structural basis of subunit stoichiometry and to identify the PSBD of E2 as the main determinant of PDHc architecture.

To simplify the biological assembly and therefore facilitate data interpretation, we followed an approach similar to that described for PDHc from *Thermoplasma acidophilum* (31) and *G. stearothermophilus* (48) and generated an E2 variant with arrested oligomerization beyond trimers. The mechanism of arrested assembly through deletion of the C-terminal two E2 residues was revealed by x-ray crystallography and cryo-EM performed on the corresponding E2 CD constructs, CD₃ and CD₂₄. The hydrophobic pocket, which is natively occupied by the last two residues of a neighboring E2 trimer, was self-complemented, preventing formation of intertrimer contacts. Breakage of the C-terminal 3₁₀-helix observed in our CD₃ crystal structure results in an extended C-terminal stretch, which is functionally reminiscent of the corresponding region in natively homotrimeric E2 found in actinobacteria (32). There, a three-residue insertion preceding the C-terminal 3₁₀-helix shifts the helix orientation, causing it to occupy the hydrophobic pocket in an intramolecular interaction. Our findings, along with the reports mentioned above, highlight the critical role of the E2 C-terminal residues in mediating intertrimer contacts, thereby determining the oligomeric state of the PDHc core complex.

Generation of the stable, trimeric E2 variant allowed us to assemble enzymatically active mini-PDHc. We characterized the association of peripheral subunits to monomeric and dimeric PSBD and found differences that imply modulation of binding affinities of E1 and E3 dependent on the oligomeric state of PSBD. While E1 dimers associate preferentially with dimeric PSBD, E3 dimers only bind monomeric PSBD. Furthermore, given that E1 is only capable of displacing E3 from the E3:E2 subcomplex carrying the wild-type (dimerization-competent) PSBD, a synergistic effect between binding of peripheral subunits and PSBD dimerization may be present. It is conceivable that PSBD dimerization ensures accommodation of both E1 and E3, and thus PDHc activity, should the relative intracellular concentrations of the peripheral subunits change.

In the 24-meric E2 core, the dimerization of PSBDs belonging to neighboring trimers is prevented by their spatial organization around the cubic CD₂₄ architecture. Within a single E2 trimer, the N termini of the CDs converge at the threefold symmetry axis of the E2 trimer. The distance between the corresponding threefold symmetry centers of neighboring vertices is ~90 Å, rendering the formation of intertrimer PSBD dimers within the same PDHc complex impossible (fig. S10A). Moreover, constraining the linkers to emerge from the center of trimers increases the local PSBD concentrations (fig. S10B), facilitating PSBD dimerization while leaving the third PSBD monomeric. This could also explain the crowding of flexibly tethered peripheral subunits around the E2 vertices previously reported by Murphy and Jensen (37) and Škerlová *et al.* (14).

Our SEC experiments demonstrated that all 24 binding sites of E2₂₄ can be occupied with a mixture of E1 and E3, whereas only 93 and 75% saturation can be reached in the presence of only E1 or E3, respectively. Single-particle cryo-EM analyses on the saturated and BS³-crosslinked E1:E2₂₄ and E3:E2₂₄ subcomplexes suggest different diameters for the peripheral protein shell formed by E1 alone or E3

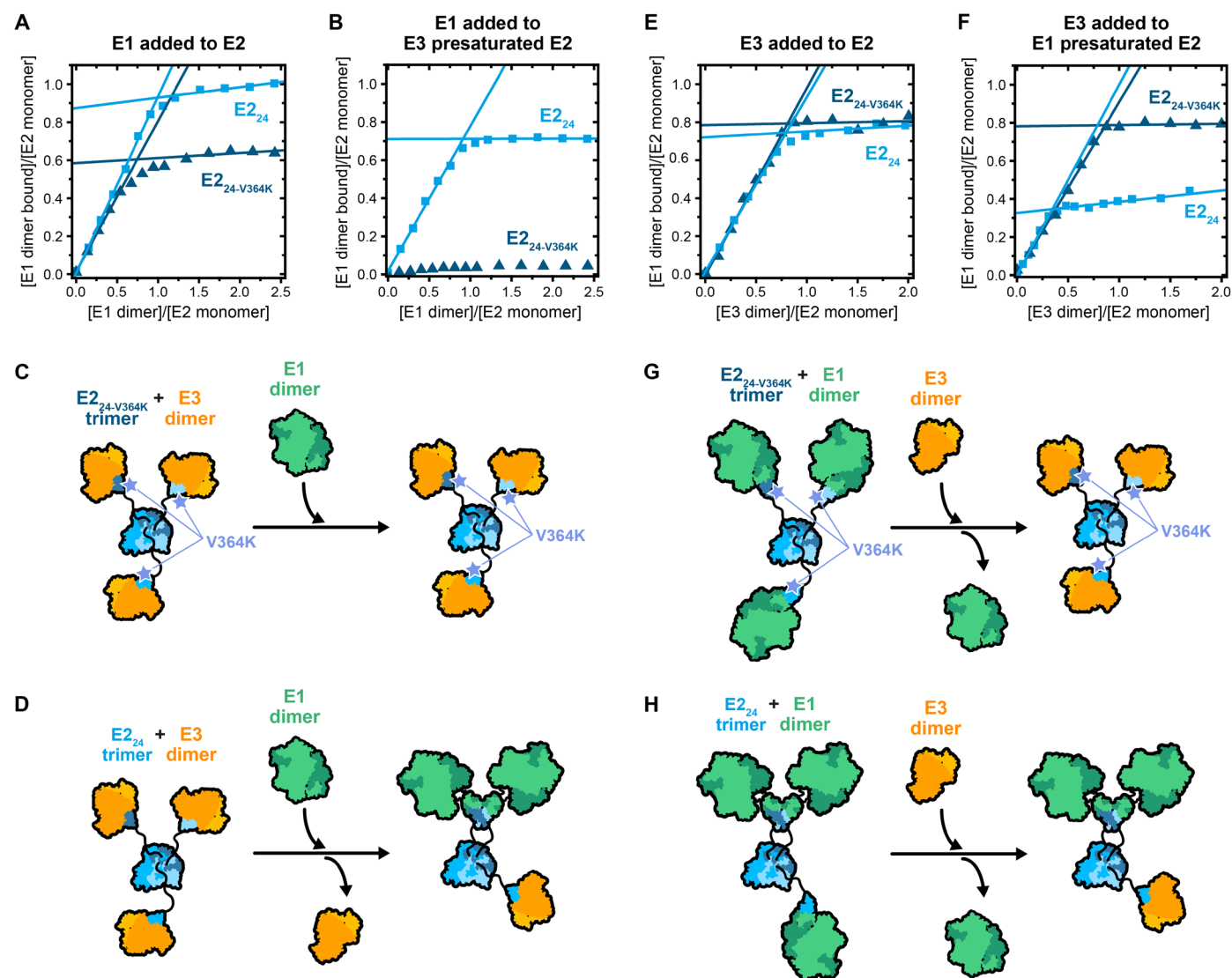


Fig. 7. Effects of the V364K substitution in the PSBD domain on the stoichiometry of E1 and E3 binding. (A, B, E, and F) Titration of the E2₂₄ and E2_{24-V364K} variants with E1 and E3, analyzed by analytical SEC. The ratio of E1/E3 dimers bound per E2 monomer is plotted against the respective ratio of E1 or E3 dimers added per E2 monomer (ratio of ligands per binding site). The ratio of E1/E3 dimers bound per E2 monomer was calculated from the peak areas of complexed subunits, determined from chromatograms recorded at 280 nm [(A) and (B)] or 450 nm (FAD in E3) [(E) and (F)], and normalized using the total peak area as a calibration curve. The data obtained for E2₂₄ is shown in light blue squares, and those for E2_{24-V364K} is shown in dark blue triangles. (C, D, G, and H) Schemes summarizing the results of the titration experiments in which preformed complexes between E2 trimers and either E1 or E3 were titrated with E3 or E1, respectively. The purple star indicates the V364K substitution within the PSBD of E2. E1 dimers are depicted in green, E3 dimers are depicted in orange, and E2 trimers are depicted in blue.

alone (fig. S11). Specifically, the analysis of 2D class averages yielded broad distance distributions with mean distances between peripheral subunits and the CD₂₄ core of ~32 Å for E1 and ~15 Å for E3. While E1 dimers appear to bind further away from the E2 core, greatly expanding the overall volume of the particle, dimers of E3 tend to associate closer to the E2 surface. This discrepancy could be attributed to the monomeric nature of E3-bound PSBD and its corresponding linker, which is highly flexible with regions of local stiffening due to its high proline content (49). In the context of E3-bound PSBD, this linker can adopt various conformational states, as opposed to the linkers of E1-bound PSBD, whose conformational freedom might become restricted upon dimerization, causing them to

adopt a more extended state, thus increase the diameter of the protein shell formed by E1.

The discovery of intratrimeric PSBD dimers provides a structural basis for interpretation of PDHc stoichiometry and organization of the peripheral subunits around the E2 core. In this study, we could identify mini-PDHc as an asymmetric building block of the full complex and hence conclude that the subunit stoichiometry is not driven by the octahedral symmetry of the core but by the oligomeric state of PSBD. Under saturating conditions, when all binding sites are occupied with peripheral subunits, the asymmetry of the trimer-based mini-PDHc breaks the symmetry in the periphery. In this context, the three chains of an E2 trimer are likely no longer

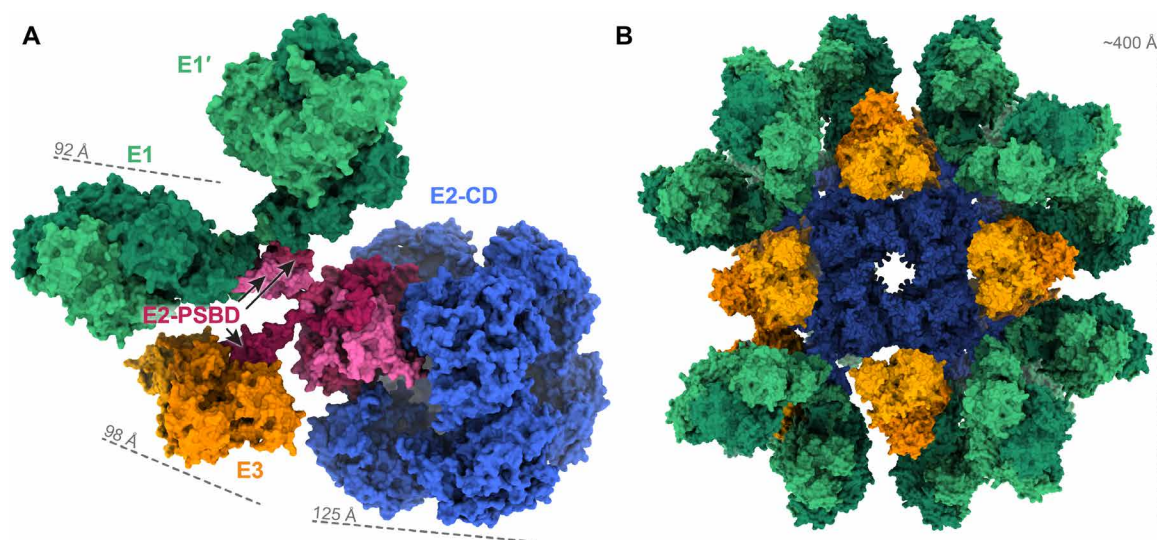


Fig. 8. Model for the organization of the peripheral subunits around the E2 core. (A) A mini-PDHc $_{\Delta LD}$ composed of trimeric PSBD-CD, two E1 dimers, and one E3 dimer was modeled based on NS-EM data (Fig. 4) and distance restraints (fig. S11) and fitted to one of the trimers of the CD $_{24}$ core. E1 dimers are shown in green, E3 dimer is shown in orange, the 24-mer of the E2 CD is shown in blue, with one trimer highlighted in red. The linkers connecting the CD and PSBD domains of the E2 trimer were modeled in Coot using geometric restraints and distances extracted from NS-EM and cryo-EM. (B) One of the possible models of fully assembled PDHc generated by fitting mini-PDHc $_{\Delta LD}$ to each of the E2 trimers in the CD $_{24}$ core. All dimeric and monomeric PSBDs are fully occupied with E1 and E3 dimers, respectively, avoiding steric clashes. LD1 to LD3 of E2 are omitted for clarity; however, the presented model allows for accommodation of all 72 LD domains.

equivalent in the catalytic cycle of PDHc. For example, dimerization of two E2 chains via PSBD might favor the reductive acetylation of the 6 LD domains from the E2 dimer and affect the previously reported interchain acetyl transfer and disulfide exchange between LDs (50–52). The transfer of reducing equivalents from LDs in the E2 dimer to the LDs in unpaired E2 might be particularly important because the three LDs from the unpaired E2 chain could be the preferred E3 substrates.

Overall, wild-type PDHc can be considered a cubic assembly of eight asymmetric mini-PDHcs, which have a defined stoichiometry but are structurally heterogeneous. This heterogeneity results not only from the flexibility of the E2 linkers but also from the stochastic dimerization of two of the three PSBDs within each of the eight E2 trimers. Although PDHc does not form a single, rigid structure, there are certain rules by which the complex assembles: (i) Each vertex of the E2 24-mer has one dimeric and one monomeric PSBD; (ii) one E3 dimer associates with monomeric PSBD, while two E1 dimers bind cooperatively (Fig. 6D, left) to dimeric PSBD, saturating the vertex; (iii) the average distance from the core is larger for E1 compared to E3 (fig. S11). Figure 8A shows a model of 24-meric E2 where one showcase vertex is saturated with E1 and E3 according to these guidelines. Such an assembly can be extrapolated to all vertices of the E2 cube, yielding a ~5.6-MDa fully saturated complex, where the exact positions of the peripheral subunits remain undefined (Fig. 8B and movie S1). The organization of the peripheral subunits around the E2 core in Fig. 8B is not static, as structural dynamics and conformational heterogeneity are essential for the biological activity of PDHc.

In conclusion, our findings provide insights into the architecture of *E. coli* PDHc, a key complex in aerobic respiration, and present a unique and previously unknown mechanism determining its composition. We confirmed that PDHc stoichiometry is not a result of simple

competitive binding of the peripheral subunits to the PSBDs of E2 but rather is determined by PSBD dimerization, which generates distinct binding sites for E1 and E3. On the basis of sequence conservation analysis, we propose that this mechanistic principle applies to PDHcs of all Gammaproteobacteria, thereby strengthening understanding of this critical metabolic enzyme in a wide range of bacterial species, including plant pathogens belonging to the *Erwinia* or *Xanthomonas* genera, as well as human pathogens such as *P. aeruginosa*, *S. enterica*, and *V. cholerae*.

MATERIALS AND METHODS

Plasmids

Genes encoding E1, E2, and E3 were amplified from an *E. coli* lysate with polymerase chain reaction (PCR) using Q5 High-Fidelity DNA polymerase (New England Biolabs). The amplified genes were cloned into the pET-21a vector via the NdeI and SacI (E2 and E3) and NheI and SacI (E1) restriction sites using T4 ligase (New England Biolabs). The CD $_{24}$ construct was derived from the E2 sequence by PCR amplification of the respective fragment followed by ligation into pET-21a. All other modifications of the different E2 variants were introduced using the QuikChange Lightning Site-Directed Mutagenesis Kit (Agilent Technologies).

Protein production and purification

Transformed *E. coli* BL21 (DE3) cells were grown with shaking at 37°C in LB-Miller medium (Becton Dickinson) with ampicillin (100 mg/liter) to an optical density OD $_{600}$ of 0.6 to 0.8. Media for production of the E2 $_{24}$ and E2 $_3$ constructs were supplemented with 1 mM (\pm)- α -lipoic acid (Sigma-Aldrich), media for E3 production were supplemented with 0.35 mM FAD (Sigma-Aldrich), and media for production of CD constructs were supplemented with additional NaCl (2 g/liter).

Protein production was induced by the addition of 0.5 mM isopropyl β -D-1-thiogalactopyranoside, and the cell suspensions were further incubated with shaking for 4 hours at 37°C (PSBD constructs) or 23 hours at 20°C (all other proteins). Frozen cell pellets were resuspended in lysis buffer [for E1: 20 mM Hepes-NaOH (pH 7.4), 150 mM NaCl, 5 mM MgCl₂, 2 mM thiamine pyrophosphate (TPP), 1 mM ethylenediaminetetraacetic acid (EDTA), and 1 mM dithiothreitol (DTT); for CD₂₄: 20 mM Hepes-NaOH (pH 7.4), 200 mM NaCl, 5 mM MgCl₂, and 5 mM CaCl₂; for all other proteins: 20 mM Hepes-NaOH (pH 7.4), 150 mM NaCl, 5 mM MgCl₂, and 5 mM CaCl₂]. Then, 1 mM phenylmethylsulfonyl fluoride, 50 μ g/ml deoxyribonuclease I, and 1 \times cComplete EDTA-free protease inhibitor cocktail (Roche) were added, and the cells were lysed by passing the suspension three times through a M110L microfluidizer (Microfluidics) at 11,000-psi chamber pressure. The lysate was centrifuged at 4°C and 48,000g for 45 min, and the supernatant was collected for further purification.

Briefly, the cleared lysates were subjected to precipitation with ammonium sulfate, followed by hydrophobic interaction chromatography, ion exchange chromatography (IEX), and SEC. The PSBD constructs were purified by incubating lysates at 75°C for 10 min, centrifuging, and subjecting the soluble fraction to IEX and SEC. For further details on protein purification, please refer to table S1. All proteins were flash-frozen and stored at -80°C in GF buffer [20 mM Hepes-NaOH (pH 7.4), 140 mM KCl, 10 mM NaCl, and 1 mM MgCl₂].

Determination of protein concentrations

The concentrations of the purified proteins were determined by measuring absorbance at 280 nm using a Cary 300 spectrophotometer (Agilent Technologies). Experimental molar extinction coefficients of the native proteins ($\epsilon_{280\text{nm}}$) were determined as described by Gill and von Hippel (53) and were: $\epsilon_{280\text{nm}}$ (E1) = 128,360 M⁻¹ cm⁻¹; $\epsilon_{280\text{nm}}$ (E₂₄) = 22,530 M⁻¹ cm⁻¹; $\epsilon_{280\text{nm}}$ (E₂₃) = $\epsilon_{280\text{nm}}$ (E_{23-V364K}) = 20,780 M⁻¹ cm⁻¹; and $\epsilon_{280\text{nm}}$ (E_{24-V364K}) = 21,080 M⁻¹ cm⁻¹. E3 concentration was determined by measuring absorbance of the FAD cofactor at 450 nm. An experimental FAD molar extinction coefficient at 450 nm of 11,170 M⁻¹ cm⁻¹ was corrected for its decrease upon binding to native E3. For all other proteins, molar extinction coefficients calculated by the Expasy ProtParam tool (54) were used.

Analytical SEC

For analytical SEC, samples were prepared in GF buffer and loaded onto a Superdex 200 Increase 5/150 GL column (Cytiva) connected to a high-performance liquid chromatography system (Agilent Technologies, 1100 Series). Chromatograms were recorded at 280 nm (protein) and/or 450 nm (FAD cofactor bound to E3).

Analytical ultracentrifugation

Freshly thawed aliquots were used for CD₃, PSBD-CD₃, and the PSBD constructs. To assemble complexes between PSBD-CD₃ and the peripheral subunits, the proteins were mixed in the following molar ratio: 0.75:1:0.35 for mini-PDHc_{ALD} (E1 dimer:PSBD-CD₃:E3 dimer) with PSBD-CD₃ at 35 μ M monomeric concentration. After incubation at room temperature for 5 min, the samples were loaded on a Superdex 200 10/300 GL column (Cytiva) to remove unbound subunits. All final samples were dissolved and diluted in GF buffer [except for the CD₃ construct in 20 mM Hepes-NaOH (pH 7.4) and 150 mM NaCl] to give absorbance between 0.05 and 1.25 at 1.2-cm

path length and a wavelength of 280 nm (samples containing PSBD-CD₃), 230 nm (PSBD constructs), or both (CD₃).

Sedimentation experiments were performed at 20°C in an Optima XL-A analytical ultracentrifuge (Beckman Coulter, USA) using analytical cells containing double-sector 12-mm charcoal-filled Epon centerpieces and quartz windows. For SV-AUC, samples with different initial protein concentrations (400 μ l) and reference buffer (420 μ l) were equilibrated at 20°C in the resting An-50 Ti rotor for at least 2 hours before acceleration to 40,000 rpm (CD₃ and PSBD-CD₃), 30,000 rpm (mini-PDHc_{ALD}), or 50,000 rpm (PSBD and PSBD-V_{364K}). Radial scans of the cells were obtained by measuring absorbance at 230 and/or 280 nm (depending on initial protein concentration), with a single acquisition in continuous mode and a step size of 0.003 cm. Data were analyzed in SEDFIT according to a continuous sedimentation coefficient distribution model [$c(s)$] (55) with frictional ratio, meniscus, and baseline as fitting parameters. Calculated sedimentation coefficient distributions were normalized using GUSI (56).

For SE-AUC experiments, samples containing the CD₃ or PSBD construct at different initial protein concentrations were successively centrifuged at 7400, 12,500, and 19,000 rpm (CD₃) or 14,000, 24,000, and 36,000 rpm (PSBD) in an An-50 Ti rotor. Sample volumes were 140 and 200 μ l for CD₃ and PSBD, respectively. For each rotor speed, radial scans were collected every 3 hours by measuring absorbance at 280 nm (CD₃) or 230 nm (PSBD), with a single acquisition in step mode and a step size of 0.001 cm. Attainment of equilibrium was assessed using the respective function in SEDFIT (57). Datasets were globally fitted using SEDPHAT (58) and assuming the presence of a single ideal species. Confidence limits for the fitted molecular mass were determined using F statistics as implemented in SEDPHAT ($P = 0.95$).

Values for buffer density, buffer viscosity, and protein partial specific volumes were calculated using SEDNTERP (59): CD₃ (0.7486 ml/g), mini-PDHc_{ALD} (0.7365 ml/g using four E1 chains, three PSBD-CD₃ chains, and two E3 chains), PSBD (0.7371 ml/g), and PSBD-V_{364K} (0.7368 ml/g).

Circular dichroism experiments

Far-UV circular dichroism spectra (205 to 255 nm) of CD₃ and CD₂₄ were recorded for 5 μ M protein samples in circular dichroism buffer [10 mM Mops-NaOH (pH 7.4), 140 mM KCl, and 10 mM NaCl] using a J-715 spectropolarimeter (Jasco). For thermal unfolding, 5 μ M CD₃ or CD₂₄ were prepared in circular dichroism buffer, and the melting curves were recorded at 222 nm with a heating rate of 1°C/min between 25° and 95°C. To determine the apparent melting temperature T_m , the data were fitted as described by Pace *et al.* (60) using the OriginPro 2018 software (OriginLab) assuming a two-state model.

Crystallization, x-ray data collection, and analysis

Crystallization plates for sitting drop vapor diffusion were set up at 21°C. The stock of 350 μ M (9.5 mg/ml) CD₃ in GF buffer was mixed at a 1:1 ratio with precipitant solution and incubated at 4°C. Crystals grew within 9 days in 100 mM tris-HCl (pH 8.5), 200 mM MgCl₂, and 30% (w/v) polyethylene glycol (PEG) 4000; they were fished from the drop and directly flash-frozen. PSBD was concentrated to 3.25 mM (24 mg/ml) in GF buffer, and crystallization plates were set up and incubated at 20°C with 1:1 mixing ratio with precipitant solution. Crystals grew within a week in 100 mM sodium acetate (pH 5.0), 2 mM ZnCl₂, and 24% (w/v) PEG 6000. As cryoprotectant,

15% glycerol was added directly to the drop before the fished crystals were flash-frozen in liquid nitrogen.

X-ray diffraction data were recorded at the X06DA beamline (PXIII) at the Swiss Light Source (Paul Scherrer Institute, Villigen, Switzerland). The data were indexed and scaled using XDS (61). Phases were determined by molecular replacement using Phaser (62) in the PHENIX software package (63). The structure of *E. coli* E2 CD [PDB: 4N72 (38)] served as a search model for CD₃; the PSBD component of the E1:PSBD structure [PDB: 4QOY (21)] was used as a search model for PSBD. The models were built in Coot (64) and refined in PHENIX. Statistics are summarized in table S2, and the atomic coordinates and structure factors are deposited in the PDB under the accession codes 8OSY (CD₃) and 8OQJ (PSBD). The crystal structure of the PSBD dimer was analyzed for interface interactions using PDBePISA (40) and COCOMAPS (41).

NS-EM sample preparation and data collection

Mini-PDHc_{ΔLD} was assembled by mixing 40 μM PSBD-CD₃ (monomeric concentration) with 30 μM E1 dimer and 15 μM E3 dimer in GF buffer. After 5-min incubation at room temperature, the sample was applied to a Superdex 200 Increase 5/150 GL column (Cytiva) equilibrated in GF buffer. The collected sample was diluted to 55 nM mini-PDHc_{ΔLD}. E1:PSBD was prepared from 10 μM PSBD (monomeric concentration) and 12.5 μM E1 dimer. The samples were incubated for 5 min at room temperature and injected onto Superdex 200 10/300 GL column (Cytiva) equilibrated in GF buffer. The sample was diluted to 35 nM E1:PSBD complexes.

NS-EM grids were prepared as previously described (65). Briefly, 4 μl of the sample was applied to glow-discharged (negative, 25 mA, 30 s; PELCO easiGlow, Ted Pella) Quantifoil copper EM grid (300 mesh) coated with a carbon film. After a 1- to 2-min incubation, the sample was blotted away with a filter paper and the grid was washed in two droplets of water. The grid was then stained for 1 to 2 min in two droplets of 2% (w/v) aqueous uranyl acetate, blotted, and air-dried. NS-EM grids were imaged on Morgagni 268 (100 kV) and Tecnai F20 (200 kV, equipped with field emission gun) transmission electron microscopes (Thermo Fisher Scientific). For automated data collection, the Tecnai F20 microscope equipped with the Falcon II direct electron detector was used. Single micrographs were recorded with the EPU software (Thermo Fisher Scientific) at a dose of approximately 50 e⁻/Å² and a pixel size of 1.32 Å/pixel.

NS-EM single-particle analysis

All NS-EM datasets were processed in a similar fashion. First, the contrast transfer function (CTF) was estimated using the Patch CTF Estimation routine in cryoSPARC v3.2 (66). After removal of poor-quality micrographs, a few hundred particles were manually selected, extracted, and subjected to 2D classification. The selected 2D class averages were then used as references for automated particle picking from all the micrographs using the Template Picker. Particles were extracted (200 pixel box size, binned to 2.31 Å/pixel for mini-PDHc_{ΔLD}; 100 pixel box size, binned to 3.96 Å/pixel for E1:PSBD) and subjected to multiple rounds of 2D classification to remove false-positive picks before generating an ab initio model. The model and selected particles were used in homogenous and/or nonuniform 3D refinements in cryoSPARC. In addition, the particles were also imported (67) to Relion 3.1 (68, 69) where they were subjected to 2D classification. The generated 2D class averages revealed complexes with easily identifiable features.

Crystal structures of PDHc subunits were rigid-body fitted into the 3D maps using UCSF ChimeraX (70), starting with an orientation in which the C termini of the PSBD dimer pointed toward the N termini of CD₃. The correlation between the fitted models and maps was determined using the fitmap command at resolution of 15 Å. The distances were measured between the N termini of the E2 CDs and the N-terminal E1 helices that bind PSBD. Because of the higher orientational freedom of E3 and thus more ambiguous fit to our density, the provided E2-E3 distance was measured at the closest point between the N terminus of the E2 CD and the surface of E3.

Cryo-EM sample preparation and data collection

Cryo-EM datasets were recorded for two constructs: CD₂₄ and mini-PDHc_{ΔLD} (E1:PSBD-CD₃:E3). CD₂₄ was diluted to 66 nM complex concentration. For mini-PDHc_{ΔLD}, the complex was prepared by mixing 12 μM PSBD-CD₃ (monomeric concentration), 8.1 μM E1 dimer, and 4.2 μM E3 dimer in GF buffer followed by a 5-min incubation at room temperature. The 1 μM mini-PDHc_{ΔLD} was then chemically fixed with an amine-reactive crosslinker via incubation with 3 mM BS³ (Thermo Fisher Scientific) for 30 min at room temperature. The unreacted crosslinker was quenched by addition of 50 mM tris-HCl (pH 8.0) and incubation for 15 min at room temperature. Crosslinking and quality of the sample were assessed with SDS polyacrylamide gel electrophoresis and NS-EM. BS³-crosslinked mini-PDHc_{ΔLD} complexes were then diluted to 125 nM before plunge-freezing on Quantifoil R2/2 holey carbon copper grids using a Vitrobot Mark IV (Thermo Fisher Scientific) and the “floating carbon” technique (71, 72). Briefly, a thin (1- to 1.5-nm) carbon film was floated on sample for 1 min, recovered with the grid, and quickly mounted in the Vitrobot set to 4°C and 100% humidity. A total of 5 μl of buffer was then applied on the carbon side, blotted for 1 to 4 s, and plunge-frozen in liquid ethane.

The cryo-EM data were recorded on two Titan Krios transmission electron microscopes (300 kV; Thermo Fisher Scientific) equipped with either K2 Summit (CD₂₄) or K3 direct electron detectors (mini-PDHc_{ΔLD}), operating in counting mode, and using a slit width of 20 eV on a GIF-Quantum energy filter (Gatan). EPU software was used for the automated data collection (Thermo Fisher Scientific). The CD₂₄ dataset of ~3600 movies was recorded with a final pixel size of 0.84 Å/pixel and a dose of 80 e⁻/Å². The data for mini-PDHc_{ΔLD} (~9300 movies) were collected with the same dose and a pixel size of 0.66 e⁻/Å². For both datasets, the defocus was set between -1.4 and -2.8 μm with 0.2-μm increments.

Cryo-EM single-particle analysis

Early processing steps were identical for the cryo-EM datasets of CD₂₄ and mini-PDHc_{ΔLD}. First, the motion-corrected and dose-weighted [MotionCor2 (73)] movies were imported into cryoSPARC v3.2 where the Patch CTF Estimation was used to estimate the CTF, astigmatism, and relative ice thickness. After removal of poor-quality micrographs, a few hundred particles were manually picked to generate 2D templates. Selected 2D class averages were used for automated particle picking from 100 randomly chosen micrographs using the Template Picker. After extraction and 2D classification, 2000 selected particles and 100 micrographs were used to train the Topaz model (74, 75). Using the trained model, particles were automatically picked from all micrographs, extracted, and subjected to multiple rounds of 2D classification to remove false-positive

picks. Dependent on the dataset, the next steps of processing were adjusted according to the complex investigated.

The CD₂₄ dataset of ~350,000 particles (256 pixel box size; 1.18 Å/pixel) was processed in cryoSPARC v3.2. Because of limited particle orientations, octahedral symmetry was imposed starting from an ab initio model and was kept throughout the processing. The initial reference and particles were subjected to heterogeneous refinement with two classes and default parameters. The final non-uniform refinement was performed on approximately 280,000 selected particles using dynamic masking and refinements of CTF and per-particle defocus. The map at 3.3-Å resolution, filtered based on local resolution estimates in cryoSPARC, was used for model refinements. A monomer of *E. coli* E2 (PDB: 4N72) was rigid-body fitted to the filtered map in UCSF Chimera (76) and real-space refined in PHENIX with standard parameters using protein secondary structure and side-chain rotamer restraints. After manual real-space refinement in Coot to reduce clashscore and rotamer outliers, an octahedral symmetry was applied to generate the 24-meric complex, which then underwent a final refinement using noncrystallographic symmetry, protein secondary structure, and side-chain rotamer restraints. The model statistics were generated with MolProbity (77) using the comprehensive validation tool in PHENIX.

The mini-PDHc_{ΔLD} dataset was processed in cryoSPARC v3.2 and Relion 3.1. First, extracted particles (200 pixel box size; 1.98 Å/pixel) were subjected to two rounds of 2D classification in cryoSPARC. Upon selection of 2D class averages (~570,000 particles), particles were imported into Relion where they underwent one more 2D classification, resulting in a pool of approximately 330,000 particles. A single initial model was created in Relion and used in 3D autorefinement with default parameters. The roughly aligned particles were subjected to 3D classification (one class, global angular searches, regularization parameter $T = 25$) using the previous map from 3D refinement as reference and a mask created in Relion, which covered a single E1 dimer and PSBD (E1-PSBD mask). Upon completion, handedness of the output map was flipped, the mask covering a single E1 dimer plus PSBD was adjusted to the new map, and the 3D classification with analogous parameters was performed. This procedure of mask adjustment and 3D classification was repeated two more times for best angular assignment. Next, the particles underwent 3D autorefinement (E1-PSBD mask; global angular searches), which reconstructed the E1 density at ~4-Å resolution. The particles were then re-extracted with 250 pixel box size and binned to 1.58 Å/pixel before being subjected to another 3D autorefinement with local angular searches and the E1-PSBD mask. The particles underwent signal subtraction using the mask on the aligned E1 dimer and PSBD, preserving their density and removing the noisy signal of misaligned CD₃ and the second dimer of E1. The signal-subtracted particles (180 pixel box size, 1.58 Å/pixel) and their corresponding 3D reconstruction were then imported back into cryoSPARC for further processing. The nonuniform refinement, with the imported 3D volume used as a reference and the E1-PSBD mask created in cryoSPARC, was performed. A mask covering only the PSBD density was then generated from the volume-erased (UCSF Chimera) map of the previous refinement and used in the 3D variability analysis set to cluster mode and filtering resolution at 5 Å. A single cluster of about 61,000 particles was subjected to a nonuniform refinement followed by a local refinement (10° and 5-Å local searches; E1-PSBD mask). Last, filtering of the map based on local resolution estimates in

cryoSPARC was conducted. Structures of the dimeric *E. coli* E1 (PDB: 4QOY; residues 56 to 886) and the AlphaFold prediction (42, 43) of two PSBD chains (E2, residues 314 to 379) in complex with four N-terminal helices of E1 (residues 1 to 58) were rigid-body fitted into the cryo-EM map using UCSF Chimera. Statistics are summarized in table S3, and the atomic coordinates and EM maps are deposited in the PDB and the Electron Microscopy Data Bank, respectively, under the accession codes 8ORB and EMD-17119 (CD₂₄) and EMD-17126 (mini-PDHc).

Measurement of enzymatic activity

For comparison of the enzymatic activities of wild-type PDHc and mini-PDHc, complexes were assembled from 300 nM E2₂₄ or E2₃ (monomeric concentration) and saturating concentrations of E1 and E3, according to our stoichiometry data. After 20-min incubation at room temperature, the apparent PDHc activity was measured spectroscopically according to the method described by Nemeria *et al.* (78). Specifically, the reaction was started by 25-fold rapid dilution of the complex with reaction buffer [20 mM Hepes-NaOH (pH 7.4), 140 mM KCl, 10 mM NaCl, 1 mM MgCl₂, 5 mM pyruvate, 2.5 mM NAD⁺, 0.2 mM TPP, 0.2 mM CoA, 2.6 mM DTT] using a plate reader equipped with a dispenser module (Synergy 2, Agilent BioTek). After 5-s mixing time, the conversion of NAD⁺ to NADH was followed for 40 s via the absorbance increase at 340 nm and 25°C [molar extinction coefficient of NADH at 340 nm: 6220 M⁻¹ cm⁻¹; (79)]. Initial slopes of the recorded curves were converted into initial velocity of NADH production per E2 monomer (TON/[E2 monomer]) (see fig. S3E) to normalize the activities of wild-type PDHc and mini-PDHc. The final concentrations of PDHc subunits in all assays were: E2 monomers (wild-type or mini-PDHc): 12 nM; E1 monomers: 16 nM; and E3 monomers: 8 nM. The enzymatic activity of wild-type PDHc or mini-PDHc was measured for three independent complex reconstitutions with two independent preparations each for E2₃ and E2₂₄. Enzymatic parameters of PDHc were determined by varying the concentration of one of the substrates, while the concentrations of the other substrates were kept constant (5 mM for pyruvate, 0.2 mM for CoA, and 2.5 mM for NAD⁺) (table S4). The data were analyzed using Eq. 1

$$v_i = [E_0] \cdot k_{\text{cat}} \cdot ([\text{Pyr}] / (K_M^{\text{Pyr}} + [\text{Pyr}])) \cdot ([\text{CoA}] / (K_M^{\text{CoA}} + [\text{CoA}])) \cdot ([\text{NAD}^+] / (K_M^{\text{NAD}} + [\text{NAD}^+])) \quad (1)$$

where v_i is the recorded initial velocity; $[E_0]$ is the concentration of fully assembled PDHc; $[\text{Pyr}]$, $[\text{CoA}]$, and $[\text{NAD}^+]$ are the concentrations of pyruvate, CoA, and NAD⁺, respectively; and K_M^{Pyr} , K_M^{CoA} , and K_M^{NAD} are the respective K_M values.

Determination of PDHc stoichiometry

The stoichiometry of complexes formed between E2 and the peripheral subunits was determined by addition of 0 to 12.5 μM E1 or E3 dimers to E2 at 5 μM monomeric concentration. Next, the stoichiometry of the complex comprising all protein components (E1, E2, and E3) was determined by incubating E2 variants (10 μM) for 5 min at room temperature with stoichiometric ratios of E1 or E3 found above and subsequent addition of the other peripheral subunit (0 to 12.5 μM dimer) to the twofold diluted assembled subcomplexes. To ensure full complex formation, the samples were incubated for another 10 min at 25°C before carrying out analytical SEC as described

above. The peak areas of the assembled complex and free peripheral subunits were determined using OriginPro 2018 or PeakFit (Systat Software). The sum of the peak areas (total peak area) in each individual SEC profile was plotted against the E1 dimer/E2 monomer or E3 dimer/E2 monomer ratio and used as internal calibration curve to determine the constant peak area of E2 (y-axis intercept of the calibration curve; the weak contribution of E2 to the total peak area results from its low extinction coefficient at 280 nm). After subtraction of the contribution of E2 in the high-molecular mass peak, the peak area of the peripheral subunit in complex with E2 was plotted against the respective E1 dimer (E3 dimer)/E2 monomer ratio. The intercept between the linear regression curves of the pre- and post-saturation data points yielded the equivalence point. Using the calibration curve for complexed E1, the peak area of bound E1 at the equivalence point was converted to the [E1 dimer bound]/[E2 monomer] ratio at the equivalence point. The workflow is illustrated in fig. S12. The provided standard errors (SEs) were calculated using the SEs of the linear regression curves.

Analysis of sequence conservation

The Basic Local Alignment Search Tool (BLAST; National Center for Biotechnology Information) was utilized to search for 5000 orthologous gammaproteobacterial sequences using residues 327 to 376 of *E. coli* E2 as template. Sequences that were either incomplete or not part of PDHc E2, despite high homology, were removed. The resultant set of 2175 gammaproteobacterial PSBD sequences were aligned with Clustal Omega (EMBL) and then converted into FASTA format using the EMBOSS Seqret tool (EMBL). This sequence alignment together with the crystal structure of dimeric PSBD were uploaded to the ConSurf Server (80, 81) to visualize sequence conservation in the context of a 3D model. The same alignment was also used for the WebLogo server (82) to generate a sequence logo plot.

Supplementary Materials

This PDF file includes:

Figs. S1 to S12
Tables S1 to S4
Legend for movie S1

Other Supplementary Material for this manuscript includes the following:

Movie S1

REFERENCES AND NOTES

1. L. J. Reed, Multienzyme complexes. *Acc. Chem. Res.* **7**, 40–46 (1974).
2. M. S. Patel, T. E. Roche, Molecular biology and biochemistry of pyruvate dehydrogenase complexes. *FASEB J.* **4**, 3224–3233 (1990).
3. M. S. Patel, T. E. Roche, R. A. Harris, *Alpha-keto acid dehydrogenase complexes* (Molecular and cell biology updates, Birkhäuser, Birkhäuser, 1996).
4. L. J. Reed, A trail of research from lipoic acid to α -keto acid dehydrogenase complexes. *J. Biol. Chem.* **276**, 38329–38336 (2001).
5. M. Koike, L. J. Reed, W. R. Carroll, α -Keto acid dehydrogenation Complexes. *J. Biol. Chem.* **238**, 30–39 (1963).
6. L. J. Reed, R. M. Oliver, Structure-Function Relationships in Pyruvate and α -Ketoglutarate Dehydrogenase Complexes in *Structure and Function Relationships in Biochemical Systems*, F. Bossa, E. Chiancone, A. Finazzi-Agrò, R. Strom, Eds. (Springer US, Boston, MA, 1982), pp. 231–241.
7. R. N. Perham, L. C. Packman, 2-Oxo acid dehydrogenase multienzyme complexes: Domains, dynamics, and Design. *Ann. N. Y. Acad. Sci.* **573**, 1–20 (1989).
8. J. R. Guest, S. J. Angier, G. C. Russell, Structure, expression, and protein engineering of the pyruvate dehydrogenase complex of *Escherichia coli*. *Ann. N. Y. Acad. Sci.* **573**, 76–99 (1989).
9. A. de Kok, A. F. Hengeveld, A. Martin, A. H. Westphal, The pyruvate dehydrogenase multi-enzyme complex from Gram-negative bacteria. *Biochim. Biophys. Acta.* **1385**, 353–366 (1998).
10. D. L. Bates, M. J. Danson, G. Hale, E. A. Hooper, R. N. Perham, Self-assembly and catalytic activity of the pyruvate dehydrogenase multienzyme complex of *Escherichia coli*. *Nature* **268**, 313–316 (1977).
11. M. S. Patel, N. S. Nemeria, W. Furey, F. Jordan, The pyruvate dehydrogenase complexes: Structure-based function and regulation. *J. Biol. Chem.* **289**, 16615–16623 (2014).
12. L. J. Reed, M. L. Hackert, Structure-function relationships in dihydrolipoamide acyltransferases. *J. Biol. Chem.* **265**, 8971–8974 (1990).
13. A. Mattevi, G. Obmolova, E. Schulze, K. H. Kalk, A. H. Westphal, A. de Kok, W. G. J. Hol, Atomic structure of the cubic core of the pyruvate dehydrogenase multienzyme complex. *Science* **255**, 1544–1550 (1992).
14. J. Škerlová, J. Berndtsson, H. Nolte, M. Ott, P. Stenmark, Structure of the native pyruvate dehydrogenase complex reveals the mechanism of substrate insertion. *Nat. Commun.* **12**, 5277 (2021).
15. A. Mattevi, G. Obmolova, K. H. Kalk, A. Teplyakov, W. G. J. Hol, Crystallographic analysis of substrate binding and catalysis in dihydrolipoyl transacetylase (E2p). *Biochemistry* **32**, 3887–3901 (1993).
16. B. Nagy, M. Polak, O. Ozohanics, Z. Zambo, E. Szabo, A. Hubert, F. Jordan, J. Novaček, V. Adam-Vizi, A. Ambrus, Structure of the dihydrolipoamide succinyltransferase (E2) component of the human α -ketoglutarate dehydrogenase complex (hKGDHC) revealed by cryo-EM and cross-linking mass spectrometry: Implications for the overall hKGDHC structure. *Biochim. Biophys. Acta Gen. Subj.* **1865**, 129889 (2021).
17. S. Liu, X. Xia, J. Zhen, Z. Li, Z. H. Zhou, Structures and comparison of endogenous 2-oxoglutarate and pyruvate dehydrogenase complexes from bovine kidney. *Cell Discov.* **8**, 126 (2022).
18. F. L. Kyriilis, D. A. Semchonok, I. Skolidis, C. Tüting, F. Hamdi, F. J. O'Reilly, J. Rappsilber, P. L. Kastiris, Integrative structure of a 10-megadalton eukaryotic pyruvate dehydrogenase complex from native cell extracts. *Cell Rep.* **34**, 108727 (2021).
19. B. O. Forsberg, S. Aibara, R. J. Howard, N. Mortezaei, E. Lindahl, Arrangement and symmetry of the fungal E3BP-containing core of the pyruvate dehydrogenase complex. *Nat. Commun.* **11**, 4667 (2020).
20. S. S. Mande, S. Sarfaty, M. D. Allen, R. N. Perham, W. G. J. Hol, Protein–protein interactions in the pyruvate dehydrogenase multienzyme complex: Dihydrolipoamide dehydrogenase complexed with the binding domain of dihydrolipoamide acetyltransferase. *Structure* **4**, 277–286 (1996).
21. P. Arjunan, J. Wang, N. S. Nemeria, S. Reynolds, I. Brown, K. Chandrasekhar, G. Calero, F. Jordan, W. Furey, Novel binding motif and new flexibility revealed by structural analyses of a pyruvate dehydrogenase-dihydrolipoyl acetyltransferase subcomplex from the *Escherichia coli* pyruvate dehydrogenase multienzyme complex. *J. Biol. Chem.* **289**, 30161–30176 (2014).
22. R. A. W. Frank, J. V. Pratap, X. Y. Pei, R. N. Perham, B. F. Luisi, The molecular origins of specificity in the assembly of a multienzyme complex. *Structure* **13**, 1119–1130 (2005).
23. K. Chandrasekhar, J. Wang, P. Arjunan, M. Sax, Y. H. Park, N. S. Nemeria, S. Kumaran, J. Song, F. Jordan, W. Furey, Insight to the interaction of the dihydrolipoamide acetyltransferase (E2) core with the peripheral components in the *Escherichia coli* pyruvate dehydrogenase complex via multifaceted structural approaches. *J. Biol. Chem.* **288**, 15402–15417 (2013).
24. G. J. Domingo, H. J. Chauhan, I. A. D. Lessard, C. Fuller, R. N. Perham, Self-assembly and catalytic activity of the pyruvate dehydrogenase multienzyme complex from *Bacillus stearothermophilus*. *Eur. J. Biochem.* **266**, 1136–1146 (1999).
25. L. J. Reed, F. H. Pettit, M. H. Eley, L. Hamilton, J. H. Collins, R. M. Oliver, Reconstitution of the *Escherichia coli* pyruvate dehydrogenase complex. *Proc. Natl. Acad. Sci. U.S.A.* **72**, 3068–3072 (1975).
26. K. J. Angelides, S. K. Akiyama, G. G. Hammes, Subunit stoichiometry and molecular weight of the pyruvate dehydrogenase multienzyme complex from *Escherichia coli*. *Proc. Natl. Acad. Sci. U.S.A.* **76**, 3279–3283 (1979).
27. C. A. Calacab, P. A. Frey, J. F. Hainfeld, J. S. Wall, H. Yang, *Escherichia coli* pyruvate dehydrogenase complex: Particle masses of the complex and component enzymes measured by scanning transmission electron microscopy. *Biochemistry* **24**, 2425–2431 (1985).
28. M. H. Eley, G. Namihiro, L. Hamilton, P. Munk, L. J. Reed, α -Keto acid dehydrogenase complexes: XVIII. Subunit composition of the *Escherichia coli* pyruvate dehydrogenase complex. *Arch. Biochem. Biophys.* **152**, 655–669 (1972).
29. D. L. Bates, R. A. Harrison, R. N. Perham, The stoichiometry of polypeptide chains in the pyruvate dehydrogenase multienzyme complex of *E. coli* determined by a simple novel method. *FEBS Lett.* **60**, 427–430 (1975).
30. R. N. Perham, E. A. Hooper, Polypeptide chain stoichiometry in the self-assembly of the pyruvate dehydrogenase multienzyme complex of *Escherichia coli*. *FEBS Lett.* **73**, 137–140 (1977).

31. N. L. Marrott, J. J. Marshall, D. I. Svergun, S. J. Crennell, D. W. Hough, J. M. van den Elsen, M. J. Danson, Why are the 2-oxoacid dehydrogenase complexes so large? Generation of an active trimeric complex. *Biochem. J.* **463**, 405–412 (2014).
32. E. M. Bruch, P. Vilela, L. Yang, A. Boyko, N. Lexa-Sapart, B. Raynal, P. M. Alzari, M. Bellinzoni, Actinobacteria challenge the paradigm: A unique protein architecture for a well-known, central metabolic complex. *Proc. Natl. Acad. Sci. U.S.A.* **118**, e2112107118 (2021).
33. P. Arjunan, N. Nemeria, A. Brunskill, K. Chandrasekhar, M. Sax, Y. Yan, F. Jordan, J. R. Guest, W. Furey, Structure of the pyruvate dehydrogenase multienzyme complex E1 component from *Escherichia coli* at 1.85 Å resolution. *Biochemistry* **41**, 5213–5221 (2002).
34. M. A. Robien, G. M. Clore, J. G. Omichinski, R. N. Perham, E. Appella, K. Sakaguchi, A. M. Gronenborn, Three-dimensional solution structure of the E3-binding domain of the dihydrolipoamide succinyltransferase core from the 2-oxoglutarate dehydrogenase multienzyme complex of *Escherichia coli*. *Biochemistry* **31**, 3463–3471 (1992).
35. J. D. F. Green, E. D. Laue, R. N. Perham, S. T. Ali, J. R. Guest, Three-dimensional structure of a lipoyl domain from the dihydrolipoyl acetyltransferase component of the pyruvate dehydrogenase multienzyme complex of *Escherichia coli*. *J. Mol. Biol.* **248**, 328–343 (1995).
36. T. Wagenknecht, R. Grassucci, J. Berkowitz, C. Forneris, Configuration of interdomain linkers in pyruvate dehydrogenase complex of *Escherichia coli* as determined by cryoelectron microscopy. *J. Struct. Biol.* **109**, 70–77 (1992).
37. G. E. Murphy, G. J. Jensen, Electron cryotomography of the *E. coli* pyruvate and 2-oxoglutarate dehydrogenase complexes. *Structure* **13**, 1765–1773 (2005).
38. J. Wang, N. S. Nemeria, K. Chandrasekhar, S. Kumaran, P. Arjunan, S. Reynolds, G. Calero, R. Bruh, L. Kakalis, W. Furey, F. Jordan, Structure and function of the catalytic domain of the dihydrolipoyl acetyltransferase component in *Escherichia coli* pyruvate dehydrogenase complex. *J. Biol. Chem.* **289**, 15215–15230 (2014).
39. R. A. W. Frank, C. M. Titman, J. V. Pratap, B. F. Luisi, R. N. Perham, A molecular switch and proton wire synchronize the active sites in thiamine enzymes. *Science* **306**, 872–876 (2004).
40. E. Krissinel, K. Henrick, Inference of macromolecular assemblies from crystalline state. *J. Mol. Biol.* **372**, 774–797 (2007).
41. A. Vangone, R. Spinelli, V. Scarano, L. Cavallo, R. Oliva, COCOMAPS: A web application to analyze and visualize contacts at the interface of biomolecular complexes. *Bioinformatics* **27**, 2915–2916 (2011).
42. J. Jumper, R. Evans, A. Pritzel, T. Green, M. Figurnov, O. Ronneberger, K. Tunyasuvunakool, R. Bates, A. Židek, A. Potapenko, A. Bridgland, C. Meyer, S. A. A. Kohli, A. J. Ballard, A. Cowie, B. Romera-Paredes, S. Nikolov, R. Jain, J. Adler, T. Back, S. Petersen, D. Reiman, E. Clancy, M. Zielinski, M. Steinegger, M. Pacholska, T. Berghammer, S. Bodenstein, D. Silver, O. Vinyals, A. W. Senior, K. Kavukcuoglu, P. Kohli, D. Hassabis, Highly accurate protein structure prediction with AlphaFold. *Nature* **596**, 583–589 (2021).
43. K. Tunyasuvunakool, J. Adler, Z. Wu, T. Green, M. Zielinski, A. Židek, A. Bridgland, A. Cowie, C. Meyer, A. Laydon, S. Velankar, G. J. Kleywegt, A. Bateman, R. Evans, A. Pritzel, M. Figurnov, O. Ronneberger, R. Bates, S. A. A. Kohli, A. Potapenko, A. J. Ballard, B. Romera-Paredes, S. Nikolov, R. Jain, E. Clancy, D. Reiman, S. Petersen, A. W. Senior, K. Kavukcuoglu, E. Birney, P. Kohli, J. Jumper, D. Hassabis, Highly accurate protein structure prediction for the human proteome. *Nature* **596**, 590–596 (2021).
44. Y. N. Kalia, S. M. Brocklehurst, D. S. Hipps, E. Appella, K. Sakaguchi, R. N. Perham, The high-resolution structure of the peripheral subunit-binding domain of dihydrolipoamide acetyltransferase from the pyruvate dehydrogenase multienzyme complex of *Bacillus stearothermophilus*. *J. Mol. Biol.* **230**, 323–341 (1993).
45. M. D. Allen, R. W. Broadhurst, R. G. Solomon, R. N. Perham, Interaction of the E2 and E3 components of the pyruvate dehydrogenase multienzyme complex of *Bacillus stearothermophilus*. *FEBS J.* **272**, 259–268 (2005).
46. N. Ferguson, T. D. Sharpe, P. J. Schartau, S. Sato, M. D. Allen, C. M. Johnson, T. J. Rutherford, A. R. Fersht, Ultra-fast barrier-limited folding in the peripheral subunit-binding domain family. *J. Mol. Biol.* **353**, 427–446 (2005).
47. J. S. Miles, J. R. Guest, S. E. Radford, R. N. Perham, Investigation of the mechanism of active site coupling in the pyruvate dehydrogenase multienzyme complex of *Escherichia coli* by protein engineering. *J. Mol. Biol.* **202**, 97–106 (1988).
48. T. Peng, H. Lee, S. Lim, Isolating a trimer intermediate in the self-assembly of E2 protein cage. *Biomacromolecules* **13**, 699–705 (2012).
49. J. D. Green, R. N. Perham, S. J. Ullrich, E. Appella, Conformational studies of the interdomain linker peptides in the dihydrolipoyl acetyltransferase component of the pyruvate dehydrogenase multienzyme complex of *Escherichia coli*. *J. Biol. Chem.* **267**, 23484–23488 (1992).
50. J. Song, F. Jordan, Interchain acetyl transfer in the E2 component of bacterial pyruvate dehydrogenase suggests a model with different roles for each chain in a trimer of the homooligomeric component. *Biochemistry* **51**, 2795–2803 (2012).
51. J. H. Collins, L. J. Reed, Acyl group and electron pair relay system: A network of interacting lipoyl moieties in the pyruvate and alpha-ketoglutarate dehydrogenase complexes from *Escherichia coli*. *Proc. Natl. Acad. Sci. U.S.A.* **74**, 4223–4227 (1977).
52. G. Hale, D. L. Bates, R. N. Perham, Subunit exchange in the pyruvate dehydrogenase complex of *Escherichia coli*. *FEBS Lett.* **104**, 343–346 (1979).
53. S. C. Gill, P. H. von Hippel, Calculation of protein extinction coefficients from amino acid sequence data. *Anal. Biochem.* **182**, 319–326 (1989).
54. E. Gasteiger, C. Hoogland, A. Gattiker, S. Duvaud, M. R. Wilkins, R. D. Appel, A. Bairoch, Protein Identification and Analysis Tools on the ExPASy Server, in *The Proteomics Protocols Handbook*, J. M. Walker, Ed. (Humana Press, 2005), pp. 571–607.
55. P. Schuck, Size-distribution analysis of macromolecules by sedimentation velocity ultracentrifugation and Lamm equation modeling. *Biophys. J.* **78**, 1606–1619 (2000).
56. C. A. Brautigam, Chapter Five - Calculations and publication-quality illustrations for analytical ultracentrifugation data, in *Methods Enzymol.*, J. L. Cole, Ed. (Academic Press, 2015), vol. 562, pp. 109–133.
57. P. Schuck, H. Zhao, C. A. Brautigam, R. Ghirlando, *Basic Principles of Analytical Ultracentrifugation* (CRC Press, Boca Raton, FL, 2016), pp. 1–294.
58. P. Schuck, On the analysis of protein self-association by sedimentation velocity analytical ultracentrifugation. *Anal. Biochem.* **320**, 104–124 (2003).
59. T. M. Laue, B. Shah, T. M. Ridgeway, S. L. Pelletier, Computer-Aided Interpretation of Sedimentation Data for Proteins, in *Analytical Ultracentrifugation in Biochemistry and Polymer Science*, S. E. Harding, J. C. Horton, A. J. Rowe, Eds. (Royal Society of Chemistry, Cambridge, U.K., 1992), pp. 90–125.
60. C. N. Pace, E. J. Hebert, K. L. Shaw, D. Schell, V. Both, D. Krajcikova, J. Sevcik, K. S. Wilson, Z. Dauter, R. W. Hartley, G. R. Grimsley, Conformational stability and thermodynamics of folding of ribonucleases Sa, Sa2 and Sa3. *J. Mol. Biol.* **279**, 271–286 (1998).
61. W. Kabsch, XDS. *Acta Crystallogr. D Biol. Crystallogr.* **66**, 125–132 (2010).
62. A. J. McCoy, R. W. Grosse-Kunstleve, P. D. Adams, M. D. Winn, L. C. Storoni, R. J. Read, Phaser crystallographic software. *J. Appl. Crystallogr.* **40**, 658–674 (2007).
63. P. D. Adams, P. V. Afonine, G. Bunkóczi, V. B. Chen, I. W. Davis, N. Echols, J. J. Headd, L.-W. Hung, G. J. Kapral, R. W. Grosse-Kunstleve, A. J. McCoy, N. W. Moriarty, R. Oeffner, R. J. Read, D. C. Richardson, J. S. Richardson, T. C. Terwilliger, P. H. Zwart, PHENIX: A comprehensive Python-based system for macromolecular structure solution. *Acta Crystallogr. D Biol. Crystallogr.* **66**, 213–221 (2010).
64. P. Emsley, B. Lohkamp, W. G. Scott, K. Cowtan, Features and development of Coot. *Acta Crystallogr. D Biol. Crystallogr.* **66**, 486–501 (2010).
65. M. Ohi, Y. Li, Y. Cheng, T. Walz, Negative staining and image classification — powerful tools in modern electron microscopy. *Biol. Proced. Online* **6**, 23–34 (2004).
66. A. Punjani, J. L. Rubinstein, D. J. Fleet, M. A. Brubaker, cryoSPARC: Algorithms for rapid unsupervised cryo-EM structure determination. *Nat. Methods* **14**, 290–296 (2017).
67. D. Asarnow, E. Palovcak, Y. Cheng, asarnow/pyem: UCSF pyem v0.5. (Zenodo, 2019); 10.5281/zenodo.3576630.
68. R. Fernandez-Leiro, S. H. W. Scheres, A pipeline approach to single-particle processing in RELION. *Acta Crystallogr. D Biol. Crystallogr.* **73**, 496–502 (2017).
69. J. Zivanov, T. Nakane, B. O. Forsberg, D. Kimanius, W. J. Hagen, E. Lindahl, S. H. W. Scheres, New tools for automated high-resolution cryo-EM structure determination in RELION-3. *eLife* **7**, e42166 (2018).
70. T. D. Goddard, C. C. Huang, E. C. Meng, E. F. Pettersen, G. S. Couch, J. H. Morris, T. E. Ferrin, UCSF ChimeraX: Meeting modern challenges in visualization and analysis. *Protein Sci.* **27**, 14–25 (2018).
71. A. Scaiola, F. Mangia, S. Imseng, D. Boehringer, K. Berneiser, M. Shimobayashi, E. Stüttfeld, M. N. Hall, N. Ban, T. Maier, The 3.2-Å resolution structure of human mTORC2. *Sci. Adv.* **6**, eabc1251 (2020).
72. N. de Martin Garrido, W. Fu, K. Ramlal, Z. Zhu, D. Miller, D. Boehringer, C. H. S. Aylett, Direct transfer of electron microscopy samples to wetted carbon and graphene films via a support floatation block. *J. Struct. Biol.* **213**, 107677 (2021).
73. S. Q. Zheng, E. Palovcak, J.-P. Armache, K. A. Verba, Y. Cheng, D. A. Agard, MotionCor2: Anisotropic correction of beam-induced motion for improved cryo-electron microscopy. *Nat. Methods* **14**, 331–332 (2017).
74. T. Bepler, A. Morin, M. Rapp, J. Brasch, L. Shapiro, A. J. Noble, B. Berger, Positive-unlabeled convolutional neural networks for particle picking in cryo-electron micrographs. *Nat. Methods* **16**, 1153–1160 (2019).
75. T. Bepler, K. Kelley, A. J. Noble, B. Berger, Topaz-Denoise: General deep denoising models for cryoEM and cryoET. *Nat. Commun.* **11**, 5208 (2020).
76. E. F. Pettersen, T. D. Goddard, C. C. Huang, G. S. Couch, D. M. Greenblatt, E. C. Meng, T. E. Ferrin, UCSF Chimera—A visualization system for exploratory research and analysis. *J. Comput. Chem.* **25**, 1605–1612 (2004).
77. V. B. Chen, W. B. Arendall III, J. J. Headd, D. A. Keedy, R. M. Immormino, G. J. Kapral, L. W. Murray, J. S. Richardson, D. C. Richardson, MolProbity: all-atom structure validation for macromolecular crystallography. *Acta Crystallogr. D Biol. Crystallogr.* **66**, 12–21 (2010).
78. N. Nemeria, A. Volkov, A. Brown, J. Yi, L. Zipper, J. R. Guest, F. Jordan, Systematic study of the six cysteines of the E1 subunit of the pyruvate dehydrogenase multienzyme complex from *Escherichia coli*: None is essential for activity. *Biochemistry* **37**, 911–922 (1998).
79. B. L. Horecker, A. Kornberg, The extinction coefficients of the reduced band of pyridine nucleotides. *J. Biol. Chem.* **175**, 385–390 (1948).
80. M. Landau, I. Mayrose, Y. Rosenberg, F. Glaser, E. Martz, T. Pupko, N. Ben-Tal, ConSurf 2005: The projection of evolutionary conservation scores of residues on protein structures. *Nucleic Acids Res.* **33**, W299–W302 (2005).

81. H. Ashkenazy, S. Abadi, E. Martz, O. Chay, I. Mayrose, T. Pupko, N. Ben-Tal, ConSurf 2016: An improved methodology to estimate and visualize evolutionary conservation in macromolecules. *Nucleic Acids Res.* **44**, W344–W350 (2016).
82. G. E. Crooks, G. Hon, J.-M. Chandonia, S. E. Brenner, WebLogo: A sequence logo generator. *Genome Res.* **14**, 1188–1190 (2004).
83. D. D. Jones, K. M. Stott, M. J. Howard, R. N. Perham, Restricted motion of the lipoyl-lysine swinging arm in the pyruvate dehydrogenase complex of *Escherichia coli*. *Biochemistry* **39**, 8448–8459 (2000).

Acknowledgments: We thank P. Afanasyev for support with EM data collection and analysis, M. Leibundgut for support with crystal structure determination, and J. Stanisich for revision of this manuscript. We thank S. Chesnov (Functional Genomics Center Zurich) for recording mass spectra. We also thank the Protein Crystallization Center at the University of Zurich for initial crystallization screens. The x-ray data were acquired at the Swiss Light Source (SLS) synchrotron at the Paul Scherrer Institute (PSI). Cryo-EM data were collected at the Scientific Center for Optical and Electron Microscopy at the ETH Zurich (ScopeM). We thank the ScopeM and SLS staff for technical support during data collection and P. Bachmann for IT support. **Funding:** This work was supported by the Swiss National Science Foundation (SNSF) grant 310030_201234 to R.G.

Author contributions: S.M., R.Z., C.G., and R.G. designed all experiments. S.M. and R.Z. cloned expression vectors, set up crystallization plates. S.M. purified the proteins, performed analytical SEC, circular dichroism, and enzymatic activity experiments. S.M. collected x-ray diffraction data, solved, and refined x-ray structures. R.Z. collected, processed, and analyzed NS-EM and cryo-EM data and performed PSBD sequence conservation analysis. C.G. conducted AUC experiments and analyzed the data. S.M. and R.Z. prepared the figures. All authors contributed to the writing of the manuscript. **Competing interests:** The authors declare that they have no competing interests. **Data and materials availability:** All data needed to evaluate the conclusions in the paper are present in the paper and/or the Supplementary Materials. The structural data reported in this study are available in the Electron Microscopy Data Bank and PDB under accession codes EMD-17119 (CD₂₄) and EMD-17126 (E1:PSBD within mini-PDHC_{ΔLD}) and PDB ID 8ORB (CD₂₄), 8OSY (CD₃), and 8OQJ (PSBD).

Submitted 7 July 2023

Accepted 11 January 2024

Published 7 February 2024

10.1126/sciadv.adj6358